Chapter IV
La and Sr Co-Doped Ceria, $Ce_{1-x-y}La_xSr_yO_{2-\delta}$ (Fixed Oxygen Vacancies) and its Nanocomposites

This chapter contains two sections. In section 1, effect of replacement of La^{3+} by Sr^{2+} in $Ce_{0.85}La_{0.15}O_{1.925}$ (keeping molar concentration of oxygen ion vacancies constant) on the crystal structure, microstructure and electrical properties has been discussed. The composition which shows the highest conductivity in this system has been chosen for nanocomposites. Section 2 focuses on the effect of addition of binary mixture of carbonates, $(Li_{0.52}Na_{0.48})_2CO_3$ on the phases, thermal, microstructural and electrical properties of La^{3+} and Sr^{2+} co-doped ceria.

4.1 La and Sr Co-Doped Ceria

4.1.1 Introduction

Solid oxide fuel cells (SOFCs) are considered as an alternative electric power generation systems due to high conversion efficiency, fuel flexibility and operation directly on natural gas [Yamamoto (2000); Chen (1997); Steele (2001); Holtappels et al. (2000); Tuller (2000)]. Solid electrolyte is the key component of SOFCs [Tuller (2000)]. Solid electrolytes should have numerous requirements, such as high oxide ion conductivity, negligible electronic conduction and thermodynamical stability over a wide range of temperature and oxygen partial pressure. Doped ceria is a well known material in modern ceramics because of its high oxide ionic conductivity for the fabrication of fuel cells and oxygen sensors [Minervini et al. (1999)].

Oxygen vacancies are produced in ceria on doping with aliovalent acceptor cations. These vacancies are free up to a particular concentration of the dopants. These vacancies get associated with the dopant cations beyond a particular concentration. For example, 20 mol% of rare earth dopants in CeO_2 produce sufficient concentration of oxygen vacancies in samarium doped ceria, $Ce_{0.80}Sm_{0.20}O_{1.90}$ (SDC) [Chen (1997)] and gadolinium doped ceria $Ce_{0.80}Gd_{0.20}O_{1.90}$ (GDC) systems [Steele (2001)].

If the concentration of the trivalent dopant excceds 20 mol%, then the ionic conductivity decreases due to defect association and/or clustering of oxygen vacancies. Co-doping has been reported as a novel method to increase the ionic conductivity of ceria [Holtappels et al. (2000); Tuller (2000); Mogensen et al. (2000)]. Herle et al. (1999) found that ceria co-doped with 3, 5 or 10 dopants show higher ionic conductivity than the best singly doped materials. $Ce_{0.80}Gd_{0.2-x}Pr_xO_{1.9}$ [Lubke et al. (1999)], $Ce_{0.80}Gd_{0.2-x}Sm_xO_{1.9}$ [Kim et al. (2000)] and $Ce_{0.85}Gd_{0.1}Mg_{0.05}O_{1.9}$ [Wang et al. (2004)] electrolytes show the evidence for the enhancement in the ionic conductivity due to co-doing. In the present chapter, effect of partial substitution of Sr^{2+} in place of La^{3+} in the composition, $Ce_{0.85}La_{0.15}O_{1.925}$ on the electrical properties has been reported. Nanocrystalline powders in the system, $Ce_{1-x-y}La_xSr_yO_{2-\delta}$ [(x=0.15, y=0.0; CLO15), (x=0.11, y=0.02; CL11S2), (x=0.07, y=0.04; CL7S4), and (x=0.03, y=0.06; CL3S6)] having equal molar concentration of oxygen vacancies have been prepared and characterized using DTA/TGA, XRD, SEM, EDS and electrical conductivity.

4.1.2 Results and Discussion

(a) Thermal analysis

DTA/TGA plots of as-prepared ash for the composition, CLO15 are shown in Fig. 4.1. It can be seen from TGA curve that the sample looses weight continuously in the temperature range 100-800 °C. The major weight loss occurs at 100 ºC and 700 ºC. The weight loss at 100 ºC is due to removal of adsorbed moisture. The weight loss in the temperature range 100-780 ºC is due to decomposition of carbonaceous materials present in the ash. The total weight loss in the sample is 26 wt% (starting weight of the sample is 15.3 mg). In the DTA plot, two endothermic peaks have been observed corresponding to these weight losses. One endothermic peak has been observed around 100 ºC which is ascribed to loss of adsorbed moisture. Second endothermic peak observed around 780 ºC corresponds to decomposition of organic residues. There is no exo or endothermic peak beyond 800 ºC. Therefore, the entire amount of as prepared ash in the system $Ce_{1-x-y}La_xSr_yO_{2-\{x/2+y\}}$ was calcined at 800 ºC for 4 hrs.

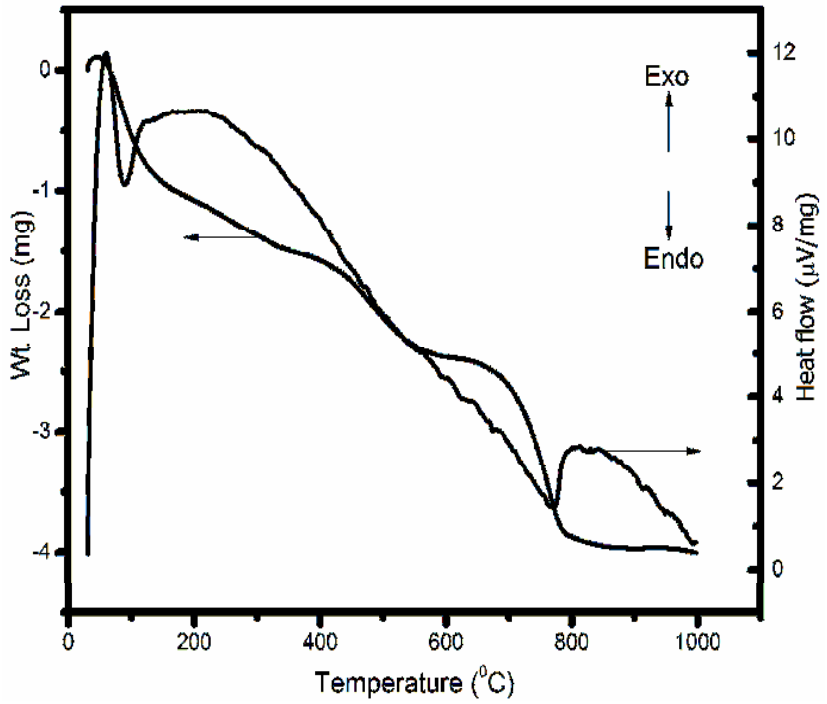

Fig. 4.1 DTA/TGA plot of the ash of composition CLO15

(b) Crystal structure and phases

Powder X-ray diffraction (XRD) patterns of all the calcined and sintered samples are recorded. Diffraction patterns are indexed on the basis of fluorite structure similar to CeO_2 with space group Fm3m using JCPDS file no. 43-1002. XRD pattern of the calcined powders is the same as that of the sintered powders except that the peaks become sharp in the case of sintered powders. Diffraction peaks of the calcined powders are broad because there is no grain growth during calcination. Average crystallite size, D, of the calcined powders, calculated by Scherrer's formula from the X-ray line broadening is given in Table. 4.1. Powder XRD patterns of all the sintered powders are shown in Fig. 4.2. The lattice constant has been determined using "Cell" software. Lattice constant increases from 5.4019+/-0.0016 Á [Singh et al. (2011)] to 5.4582+/-0.0005 Á on addition of La to CeO_2. This can be attributed to the volume expansion of the lattice due to larger ionic radius of La^{3+} (1.16 Á) than Ce^{4+} (0.97 Á). Fig. 4.2 also shows that the 2θ values of co-doped ceria shifts slightly towards higher angles with increasing Sr content. Lattice constant of the system, $Ce_{1-x-y}La_xSr_yO_{2-\{x/2+y\}}$ decreases linearly with increasing concentration of Sr^{2+} (as shown in Fig. 4.3).

This is due to decrease in the total concentration of the dopants i.e. for each mol% of Sr^{2+}, 2 mol% of La^{3+} decreases. Samples sintered at 1350 °C for 4 hrs have density more than 95% of the theoretical density (TD) (Table.4.1).

Theoretical values of lattice parameter are also calculated using hard sphere model [Hong et al. (1995)] to verify the experimental values. The results are plotted in Fig. 4.3. The radii of oxygen vacancies formed by La^{3+} and Sr^{2+} cations has also been calculated by using this model in the system $Ce_{1-x-y}La_xSr_yO_{2-\{x/2+y\}}$.

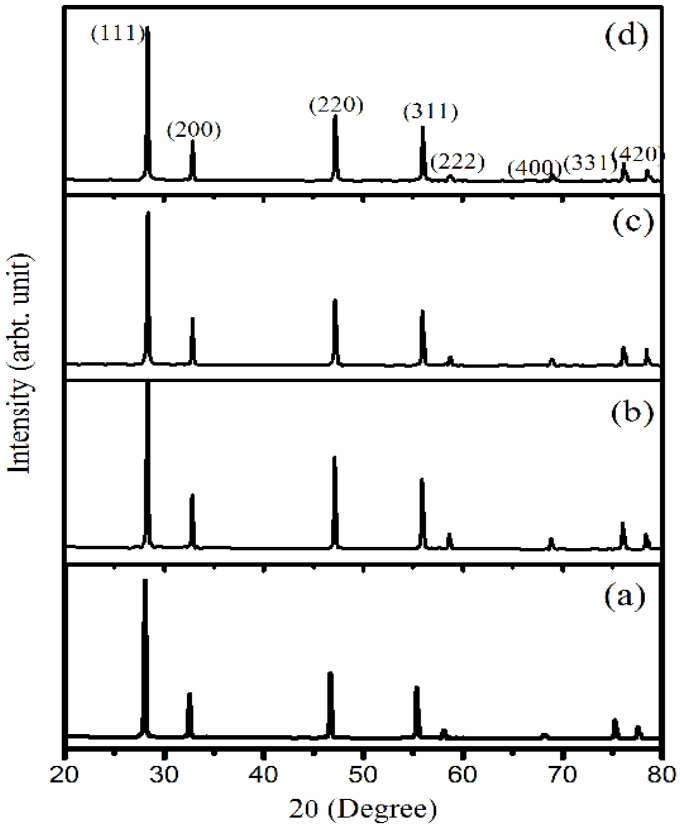

Fig. 4.2 X-ray diffraction patterns of the sintered samples of compositions (a) CLO15 (b) CL11S2(c) CL7S4 (d) CL3S6 in the system $Ce_{1-x-y}La_xSr_yO_{2-\{x/2+y\}}$

The equation for $Ce_{1-x-y}La_xSr_yO_{2-\{x/2+y\}}$ system is given as:

$$xLaO_{1.5} + ySrO + (1-x-y)CeO_2 = xLa'_{Ce} + ySr''_{Ce} + (\frac{x}{2}+y)V_{\ddot{O}} + (1\text{-}x\text{-}y)Ce_{Ce} + [2-(x/2+y)]O_O \quad (4.1)$$

where, the species are written in accordance with Kroger Vink notation of defects. Lattice parameter of an ideal fluorite structure is given as below:

$$a = \frac{4}{\sqrt{3}}(r_{anion} + r_{cation}) \quad (4.2)$$

where, r_{anion} and r_{cation} are radii of the cations and anions respectively and these are calculated using the Eq^{ns}. 4.3 and 4.4 as given below:

Table. 4.1 Crystallite size (calcined powders), lattice parameter and % theoretical density obtained of all the compositions in the system $Ce_{1-x-y}La_xSr_yO_{2-\{x/2+y\}}$

S. No.	x & y	Sample code	Crystallite size (nm)	Lattice parameter (Å)	% TD
1.	0.15 & 0.0	CLO15	21	5.4582+/-0.0005	98.3
2.	0.11 & 0.02	CL11S2	23	5.4530+/-0.0003	97.7
3.	0.07 & 0.04	CL7S4	25	5.4484+/-0.0005	95.0
4.	0.03 & 0.06	CL3S6	27	5.4445+/-0.0011	94.3

$$r_{cation} = xr_{La} + yr_{Sr} + (1-x-y)r_{Ce} \quad (4.3)$$

$$r_{anion} = \left(\frac{2-(\frac{x}{2}+y)}{2}\right)r_o + \left(\frac{\frac{x}{2}+y}{2}\right)r_{\ddot{V}_O} \quad (4.4)$$

where r_{Ce}, r_{Sr}, r_{La}, $r_{V_O^{\bullet\bullet}}$ and r_o are radii of Ce^{4+}, Sr^{2+}, La^{3+}, $V_O^{\bullet\bullet}$ and O^{2-} ion respectively. From Eq^n.4.2, the lattice parameter of lanthanum and strontium co-doped ceria system is given by:

$$a = \frac{4}{\sqrt{3}}(r_{anion} + r_{cation}) = \frac{4}{\sqrt{3}}\left[xr_{La} + yr_{Sr} + (1-x-y)r_{Ce} + \left(\frac{2-\left\{\frac{x}{2}+y\right\}}{2}\right)r_o + \left(\frac{x}{4}r_{V_{\ddot{O}_t}} + 0.5yr_{V_{\ddot{O}_d}}\right)\right] \quad (4.5)$$

By using r_{Ce} = 0.97 Å, and r_o = 1.4 Å, lattice parameter of CeO_2 is found to be 5.473 Å. Since the actual lattice parameter of pure ceria is 5.414 Å based on JCPDS files, a multiplication factor of 5.414/5.473 = 0.9892 has been taken in all of the above equations [Yeh et al. (2005)]. Hence, the Eq^{n}.4.5 is written as:

$$a = 0.9892 \times \frac{4}{\sqrt{3}}\left[xr_{La} + yr_{Sr} + (1-x-y)r_{Ce} + \left(\frac{2-\left\{\frac{x}{2}+y\right\}}{2}\right)r_o + \left(\frac{x}{4}r_{V_{\ddot{O}_t}} + 0.5yr_{V_{\ddot{O}_d}}\right)\right] \quad (4.6)$$

where $V_{O_t^{\cdot\cdot}}$ and $V_{O_d^{\cdot\cdot}}$ are oxygen vacancy produced from trivalent and divalent cations respectively. Eq^{n}.4.6 has been used to determine the theoretical value of lattice parameter for lanthanum and strontium co-doped ceria system. Lattice parameters of $Ce_{0.90}Sr_{0.10}O_{1.90}$ and $Ce_{0.85}La_{0.15}O_{1.925}$ are calculated using Eq^{ns}. 4.7 and 4.8.

(a) $Ce_{0.90}Sr_{0.10}O_{1.90}$

$$a = 0.9892 \times \frac{4}{\sqrt{3}}\left[0.90r_{Ce} + 0.10r_{Sr} + \left(\frac{1.9}{2}\right)r_o + \left(\frac{0.10}{2}\right)r_{V_{\ddot{O}}}\right] \quad (4.7)$$

(b) $Ce_{0.85}La_{0.15}O_{1.925}$

$$a = 0.9892 \times \frac{4}{\sqrt{3}}\left[0.85r_{Ce} + 0.15r_{La} + \left(\frac{1.925}{2}\right)r_o + \left(\frac{0.075}{2}\right)r_{V_{\ddot{O}}}\right] \quad (4.8)$$

Substituting the lattice parameter of $Ce_{0.90}Sr_{0.10}O_{1.90}$ (5.429 Å) and $Ce_{0.85}La_{0.15}O_{1.925}$ (5.4582 Å) in Eq^{ns}. 4.7 and 4.8, the radius of oxygen ion vacancy formed by divalent and trivalent cations are 0.9498 and 1.154 Å respectively. It is concluded that radius of oxygen vacancies formed by trivalent cations is more than that of the divalent cations. Large radius of oxygen vacancies provides easy migration of the oxide ions. The theoretical and experimental values of lattice parameters of lanthanum and strontium co-doped ceria systems are plotted as shown in Fig. 4.3.

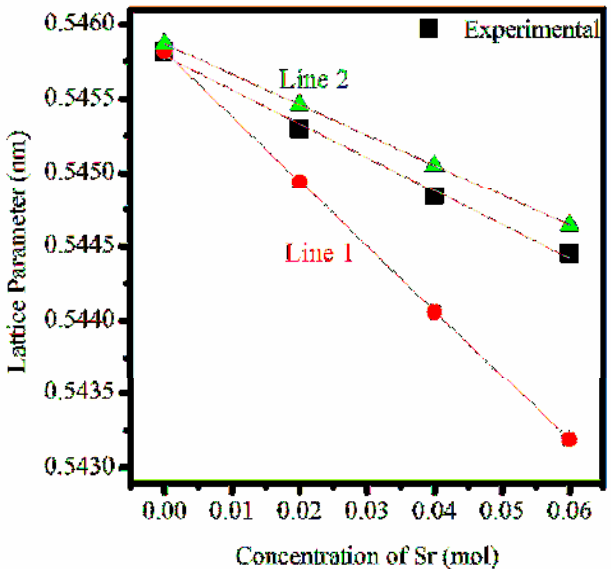

Fig. 4.3 Variation of lattice parameter as a function of Sr^{2+} concentration in the system $Ce_{1-x-y}La_xSr_yO_{2-\{x/2+y\}}$

Substituting the values of ionic radius of oxygen vacancy produced by trivalent and divalent dopant denoted by $r_{V_{O_t^{\cdot}}}$ and $r_{V_{O_d^{\cdot\cdot}}}$ as 1.154 and 0.9498 Å respectively in Eq^{n}. 4.6, the lattice parameters have been calculated and shown by the line 1 in Fig. 4.3. These calculated values are different from the experimental values. If the same value of $r_{V_{O_t^{\cdot}}}$ and $r_{V_{O_d^{\cdot\cdot}}}$ (average oxygen vacancy radius 1.16 Å) [Yeh et al. (2007)] are substituted in Eq^{n}. 4.6, the calculated values of lattice parameter are shown by line 2. These values have been found in good agreement with the experimental results. Therefore, it is found that the radii of oxygen vacancies formed by trivalent and divalent cations in lanthanum and strontium co-doped ceria systems are not different.

(c) Microstructure

Figs. 4.4 (a)-(d) show SEM micrographs of all the sintered samples. The surface micrograph reveals a dense structure and well defined grains separated by the grain boundaries. All the samples show grains of varying size. The image of all the samples except CLO15 indicates the presence of faceted grains. Faceted grain boundaries result in high lattice coherency compared to a random boundary [Cho et al. (2006)].

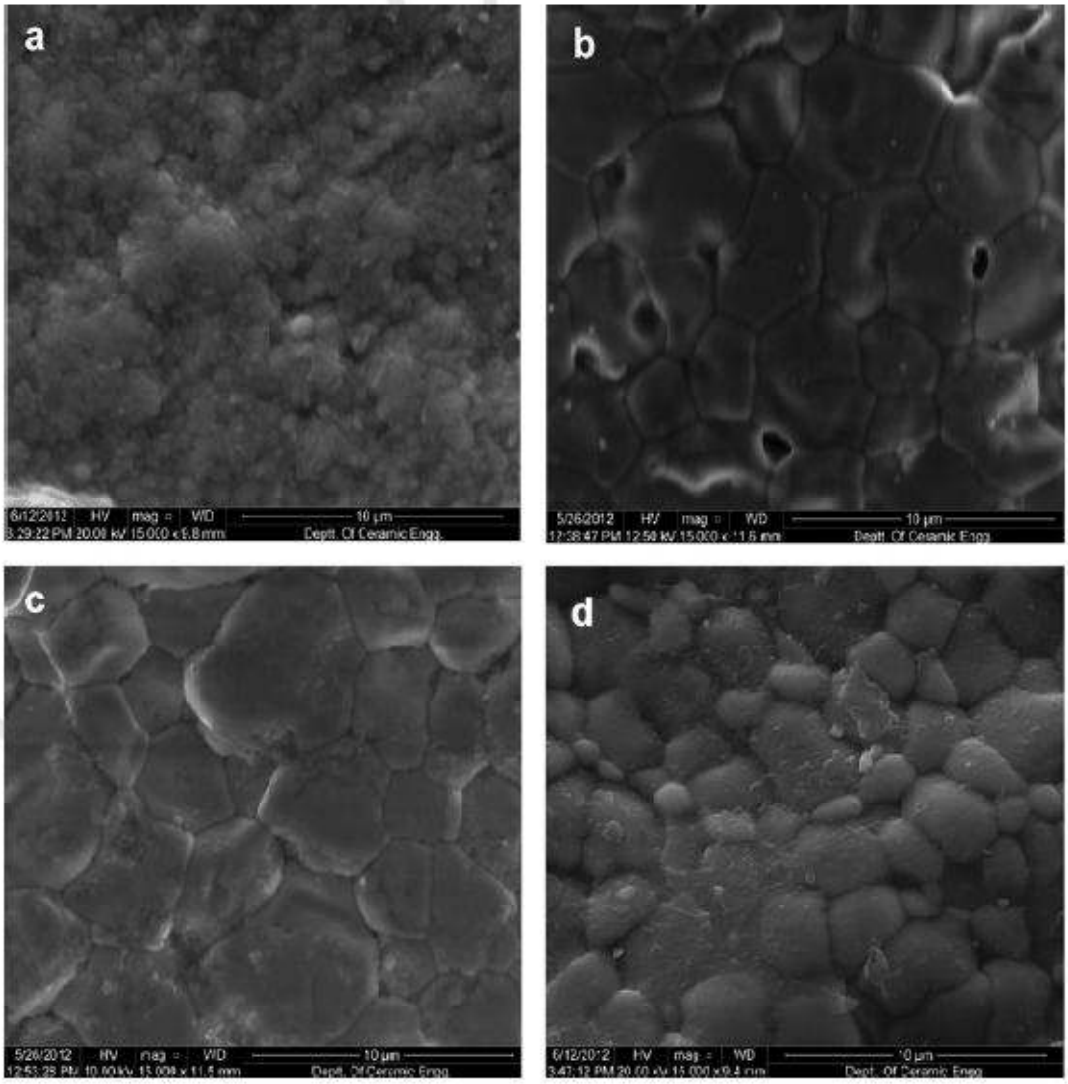

Fig. 4.4 SEM micrographs of the sintered samples of compositions (a) CLO15 (b) CL11S2 (c) CL7S4 (d) CL3S6 in the system $Ce_{1-x-y}La_xSr_yO_{2-\{x/2+y\}}$

Faceted grain boundary is an ordered state corresponding to discontinuous configuration of the siliceous phase [Cho et al. (2006)]. The average grain size for the samples CLO15, CL11S2, CL7S4 and CL3S6 has been found to be 1.0, 3.5, 4.0 and 2.9 μm respectively. EDS spectrum of the composition, CLO15 at three different points is shown in Fig. 4.5. Spectrum 1 is from a point in the grain, spectrum 2 corresponds to a point on the grain boundary and spectrum 3 is from a triple point.

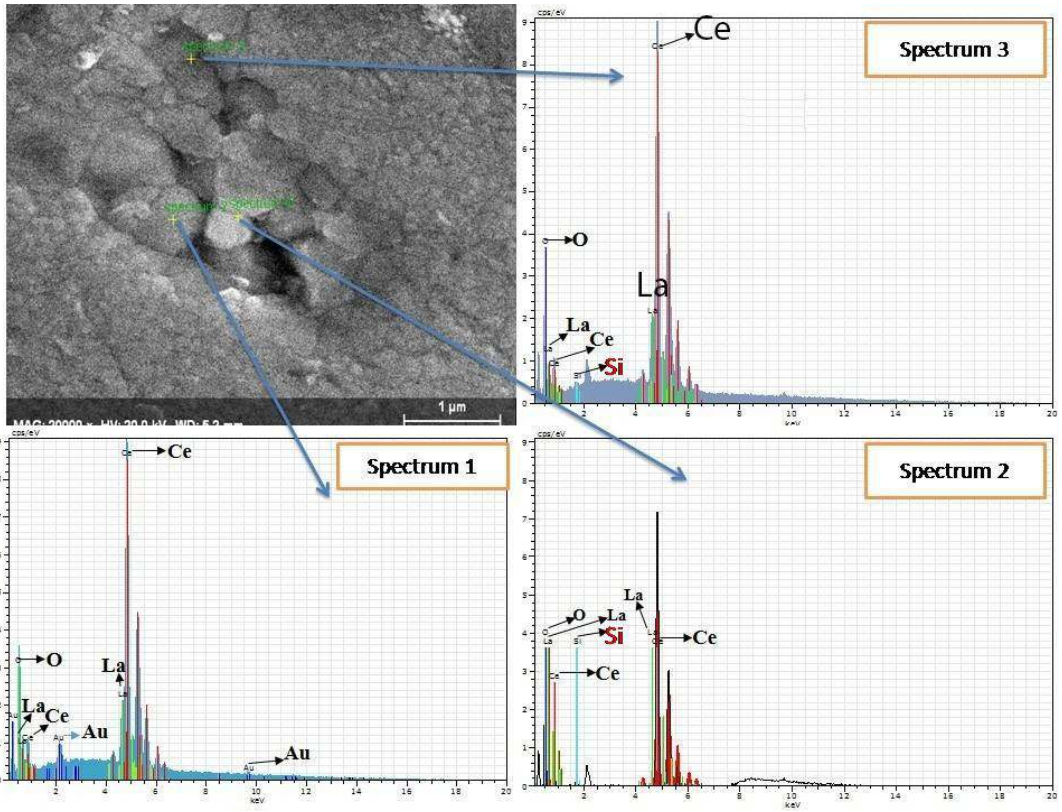

Fig. 4.5 EDS spectrum of the composition CLO15 at three points

EDS spectrum reveals that the constituent elements are present in the concentration as expected. It can be observed from Fig. 4.5 that spectrum at three points are not very different except that a second phase of silicon is present at the grain boundary and triple point. Au is also present in the spectrum. It comes due to gold coating on the sample. Fig. 4.6 shows the EDX spectrum of the composition, CL7S4 at three different points. The spectrum at three points is similar except that silicon is present at the triple point only (spectrum 3). This is because Sr reacts with silica and forms some silicate phase which segregates at the triple point. This leaves clean grain boundaries and increases grain to grain contact area for easy diffusion of oxygen ions across the grain boundaries. The composition, morphology and distribution of these phases needs to be determined using analytical studies such as; scanning transmission electron microscopy (STEM) combined with energy dispersive X-ray microanalysis (EDXM) and electron energy loss spectroscopy (EELS) [Gerhardt et al. (1986)].

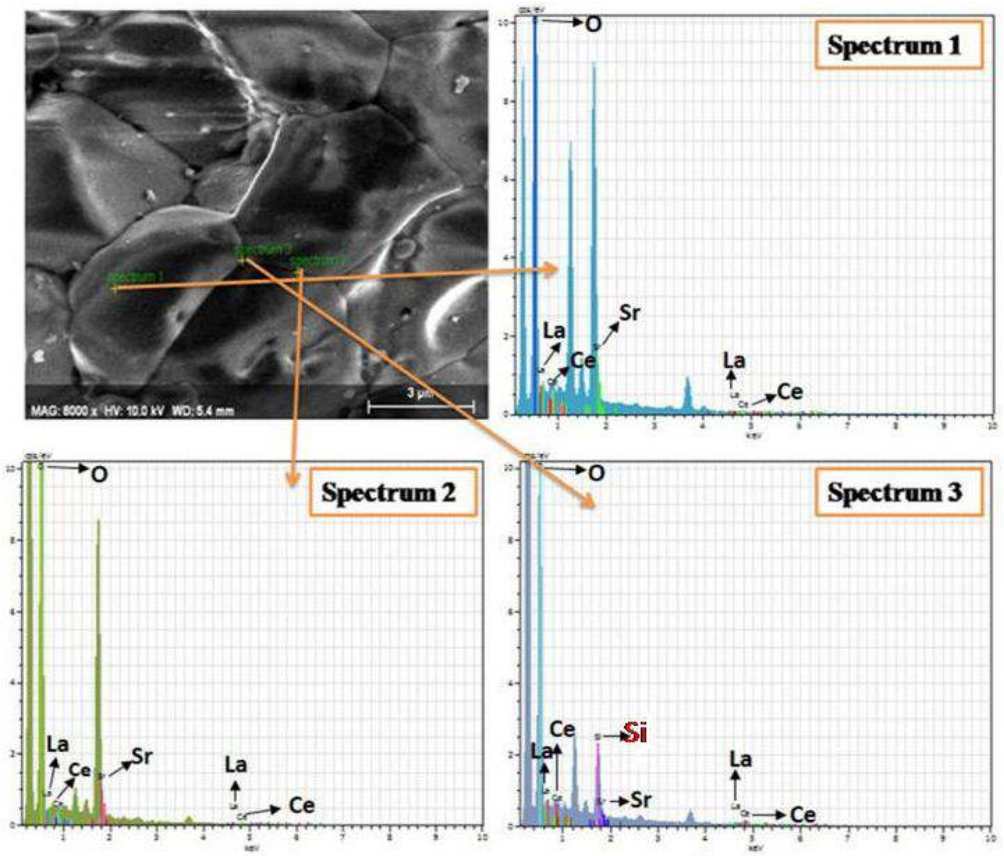

Fig. 4.6 EDS spectrum of the composition CL7S4 at three points

(d) Electrical conductivity

Complex plane impedance plots for all the compositions in the system $Ce_{1-x-y}La_xSr_yO_{2-\{x/2+y\}}$ are shown in the Figs. 4.7 to 4.10. Fig. 4.7 shows the impedance plots of CLO15 at different temperatures. In the case of CLO15, two depressed circular arcs have been observed at 200 and 225 ºC. The arc passing from the origin in the high frequency region is ascribed to the contribution of the grains to the total resistance. The intermediate frequency arc corresponds to the contribution of the grain boundaries. As the temperature increases from 250 to 325 ºC, a low frequency tail has been observed. This corresponds to electrode/specimen interface polarization. As the temperature increases, the relaxation frequency of the polarization processes increases. This causes the shifting of the arcs towards higher frequency with temperature.

The arc due to grains disappears above 325 ºC. At higher temperatures, only two arcs have been observed corresponding to the contribution of grain boundaries and electrode/specimen to the total resistance of the electrolyte. Total resistance of the sample decreases with increasing temperature.

The grains and grain boundaries arcs are associated with the capacitances in the pF (10^{-10}-10^{-12}) and nF (10^{-7}-10^{-9}) ranges respectively. These are determined from the relation $2\pi f_{max}RC = 1$, where f_{max} is the frequency at the highest point of the arc and R is the resistance and C is the capacitance of a particular contribution [Hodge et el. (1976)].

Impedance plots are fitted to an equivalent circuit as shown in the Figs. 4.7-4.10. In the present investigation, sum of the resistance of the grains and the grain boundaries is taken as the total resistance of the sample. Therefore, only arcs of the grains and the grain boundaries are fitted to obtain the best fitting with minimum error. The arc of electrode is not fitted. The accuracy of the impedance data is shown by the error bar in the plots.

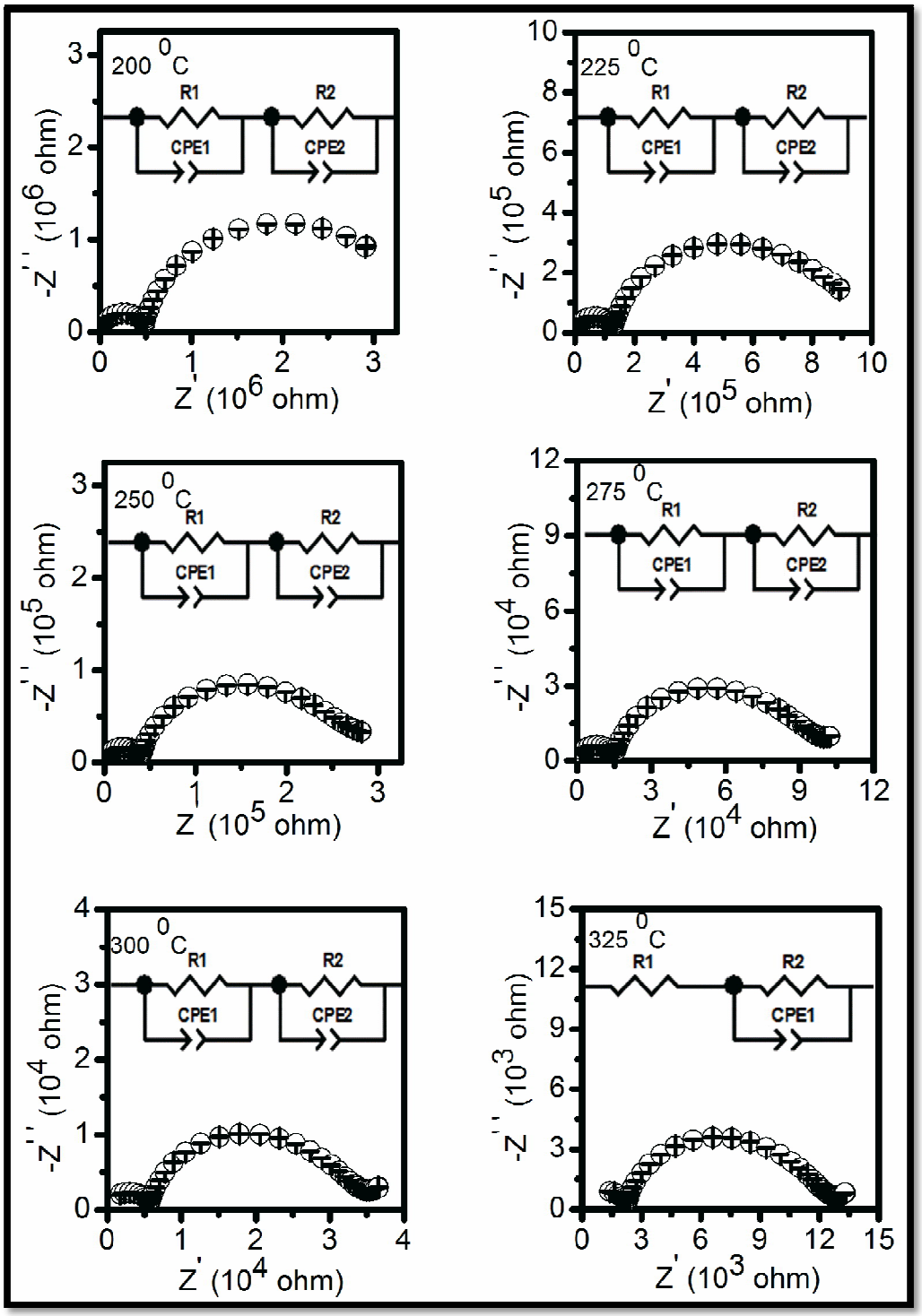

Fig. 4.7 Complex plane impedance plots of the composition CLO15 at different temperatures

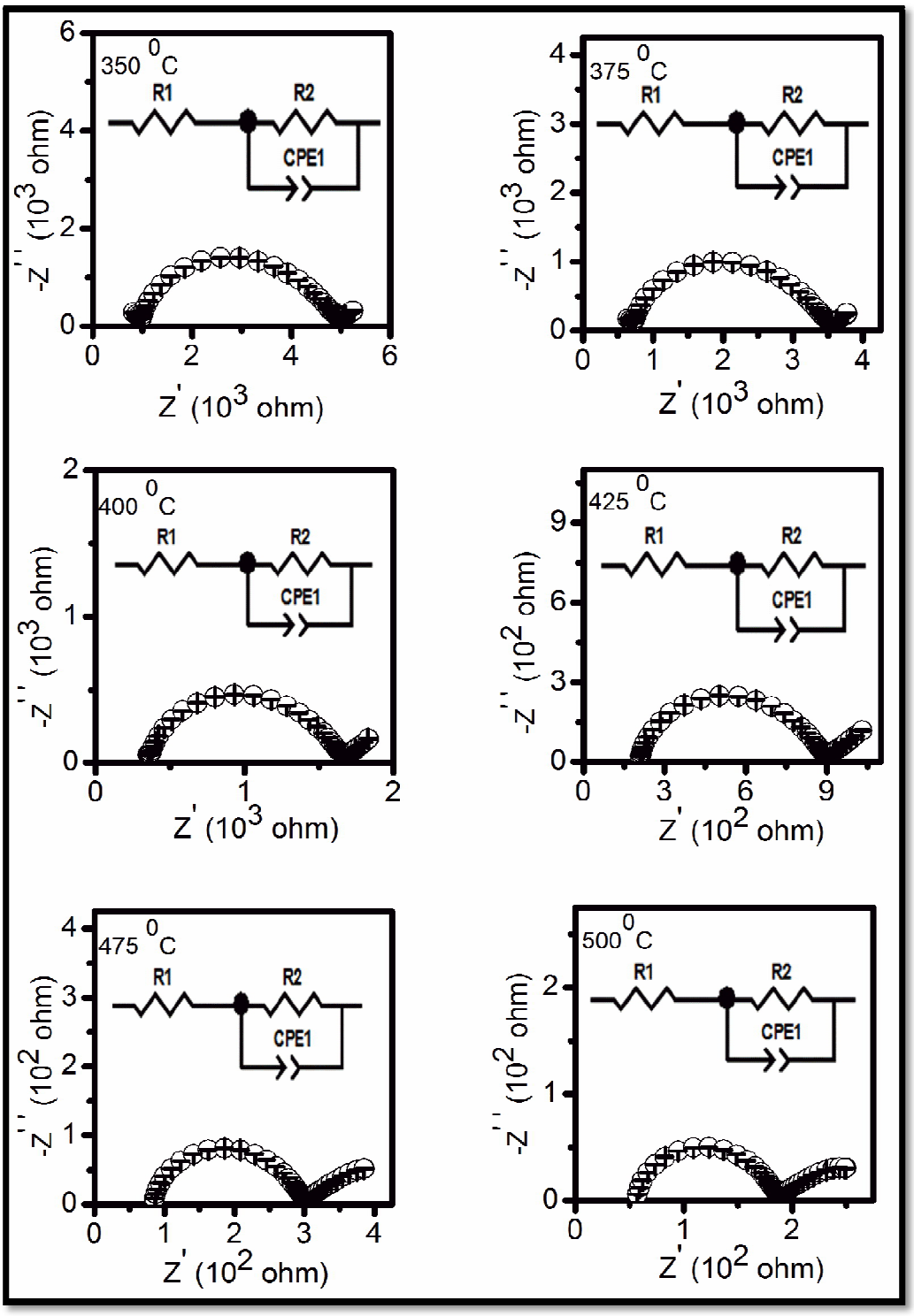

Fig. 4.7 Complex plane impedance plots of the composition CLO15 at different temperatures

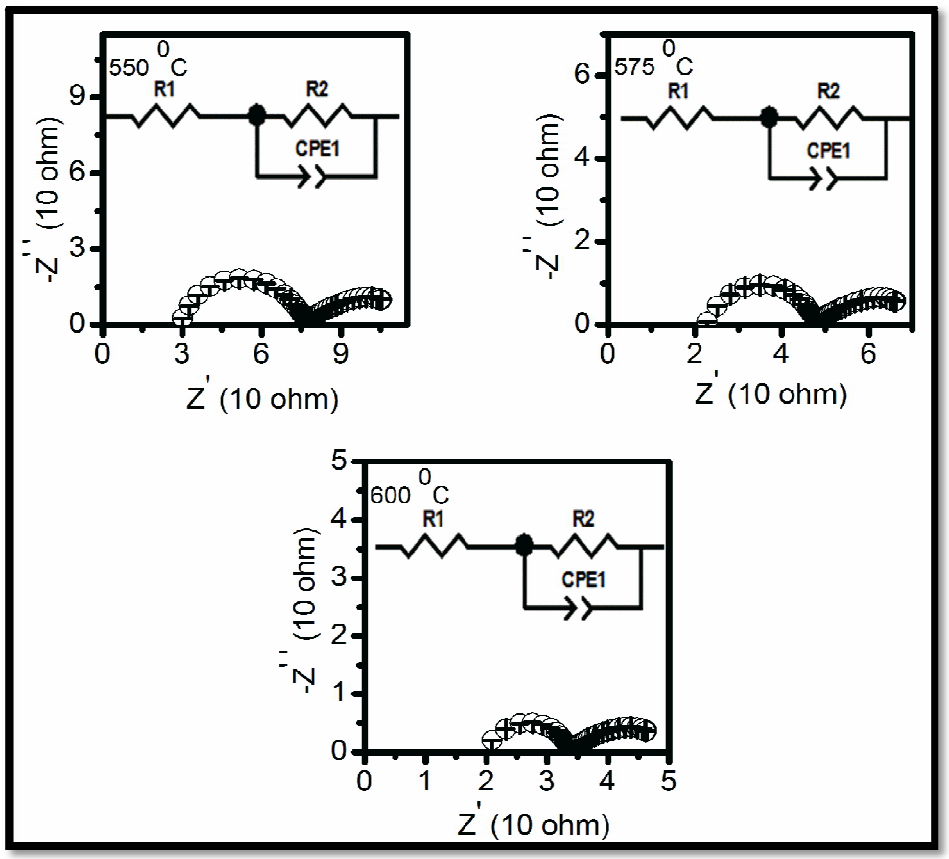

Fig. 4.7 Complex plane impedance plots of the composition CLO15 at different temperatures

For the composition CL11S2, three depressed arcs have been observed in the high, intermediate and low frequency region corresponding to the contribution of the grains, grain boundaries and electrode/electrolyte interface to the total resistance. The arcs due to grains and grain boundaries disappear above 275 and 475 ºC respectively. Only the low frequency arc has been observed at higher temperature. As the temperature increases, the total resistance decreases. It is noted form Figs. 4.8 that the area of the grain boundaries arc is less than that in CLO15. For CL7S4, three circular arcs have been observed in the temperature range 200-275 ºC. The high frequency arc is ascribed to the contribution of the grains, intermediate frequency arc to the grain boundaries and the low frequency tail is ascribed to the contribution of the electrode/specimen interface polarization.

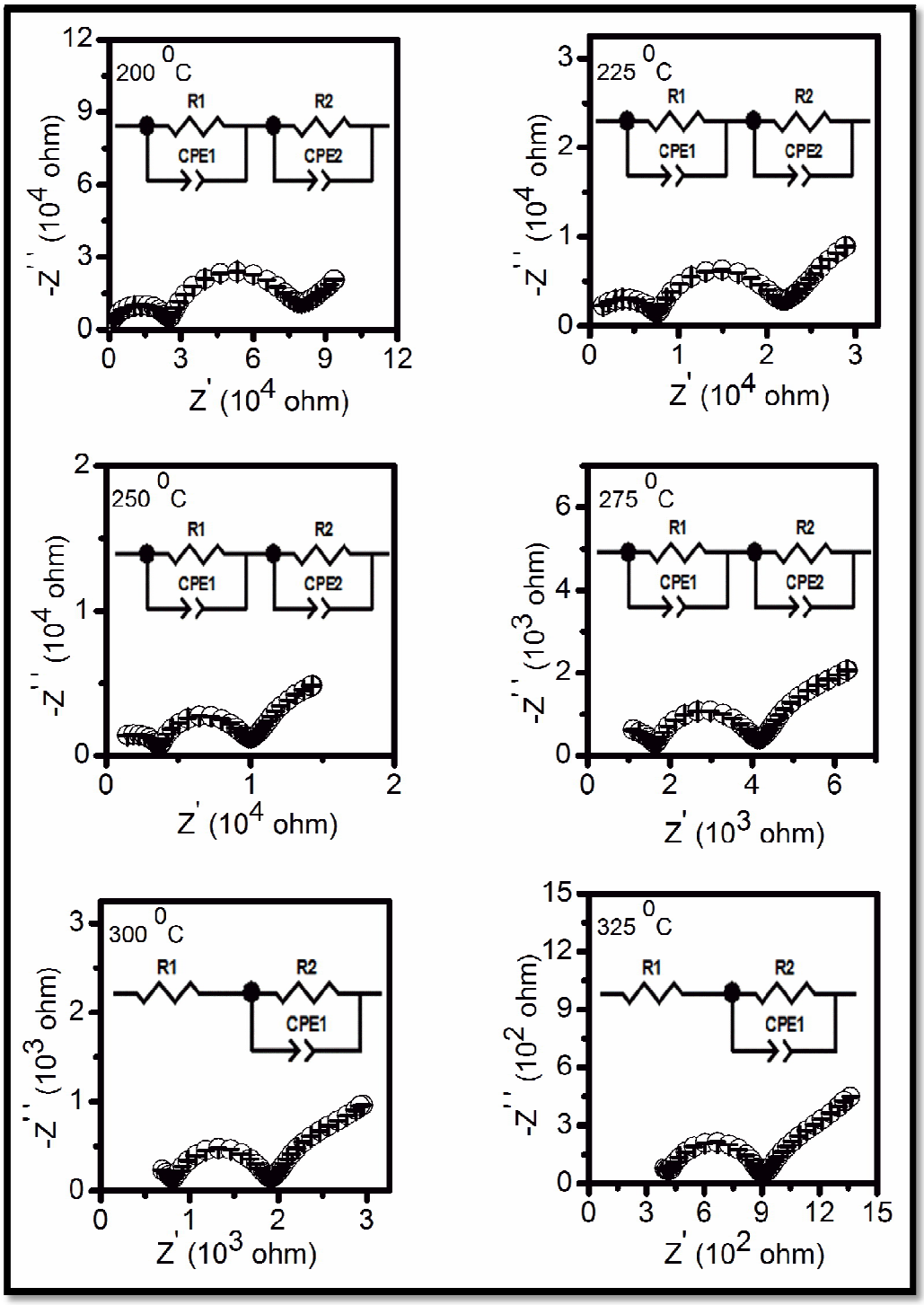

Fig. 4.8 Complex plane impedance plots of the composition CL11S2 at different temperatures

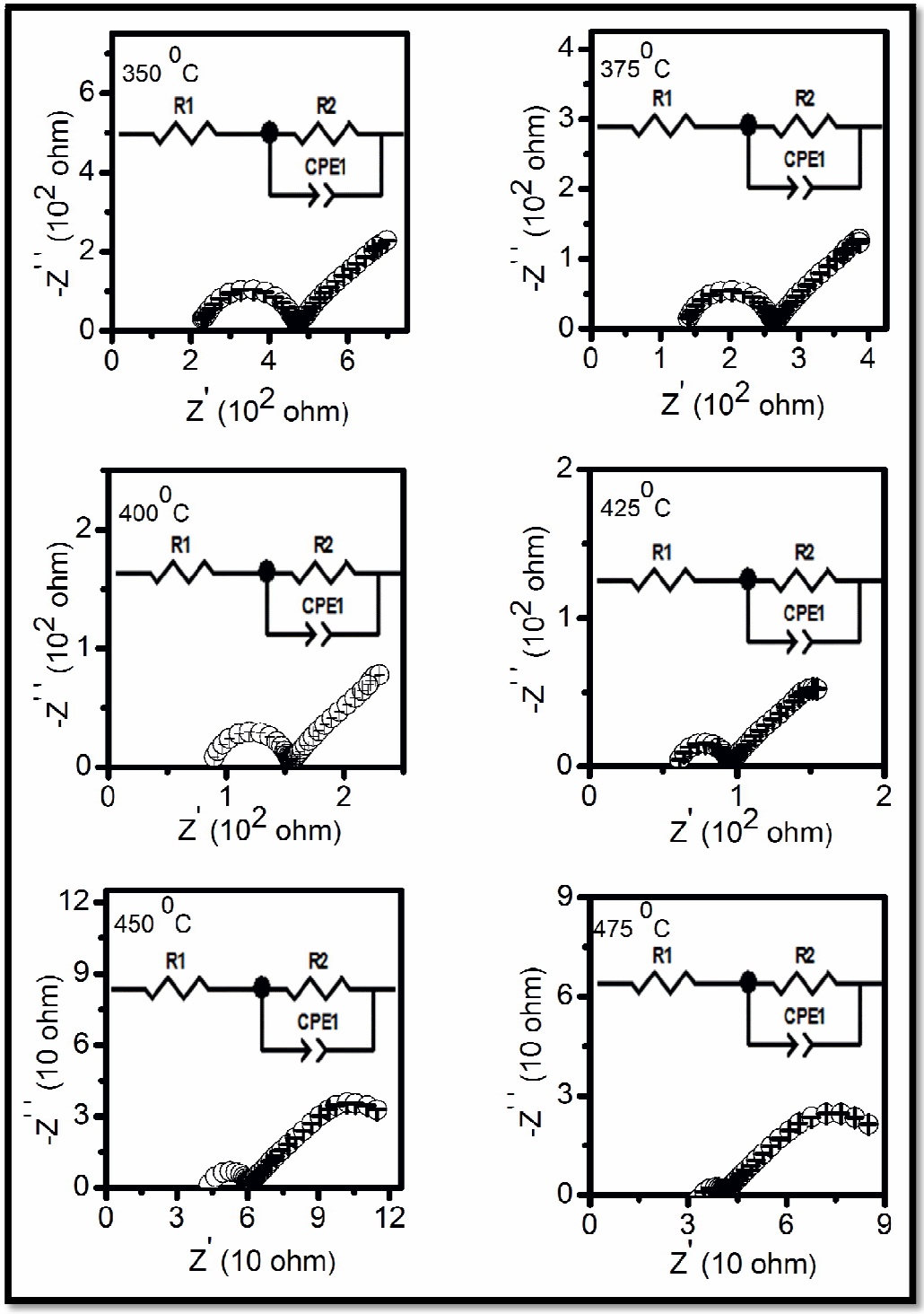

Fig. 4.8 Complex plane impedance plots of the composition CL11S2 at different temperatures

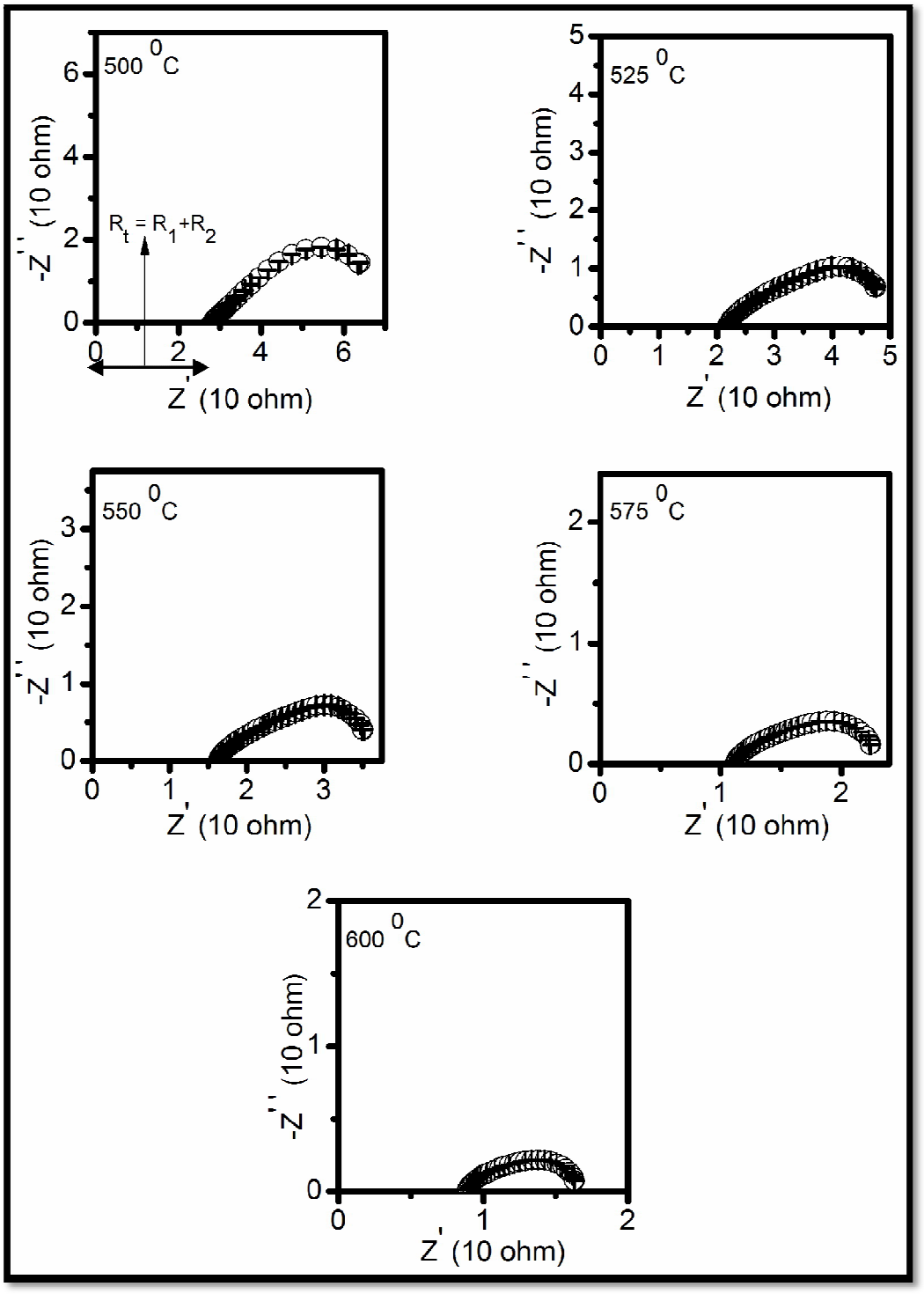

Fig. 4.8 Complex plane impedance plots of the composition CL11S2 at different temperatures

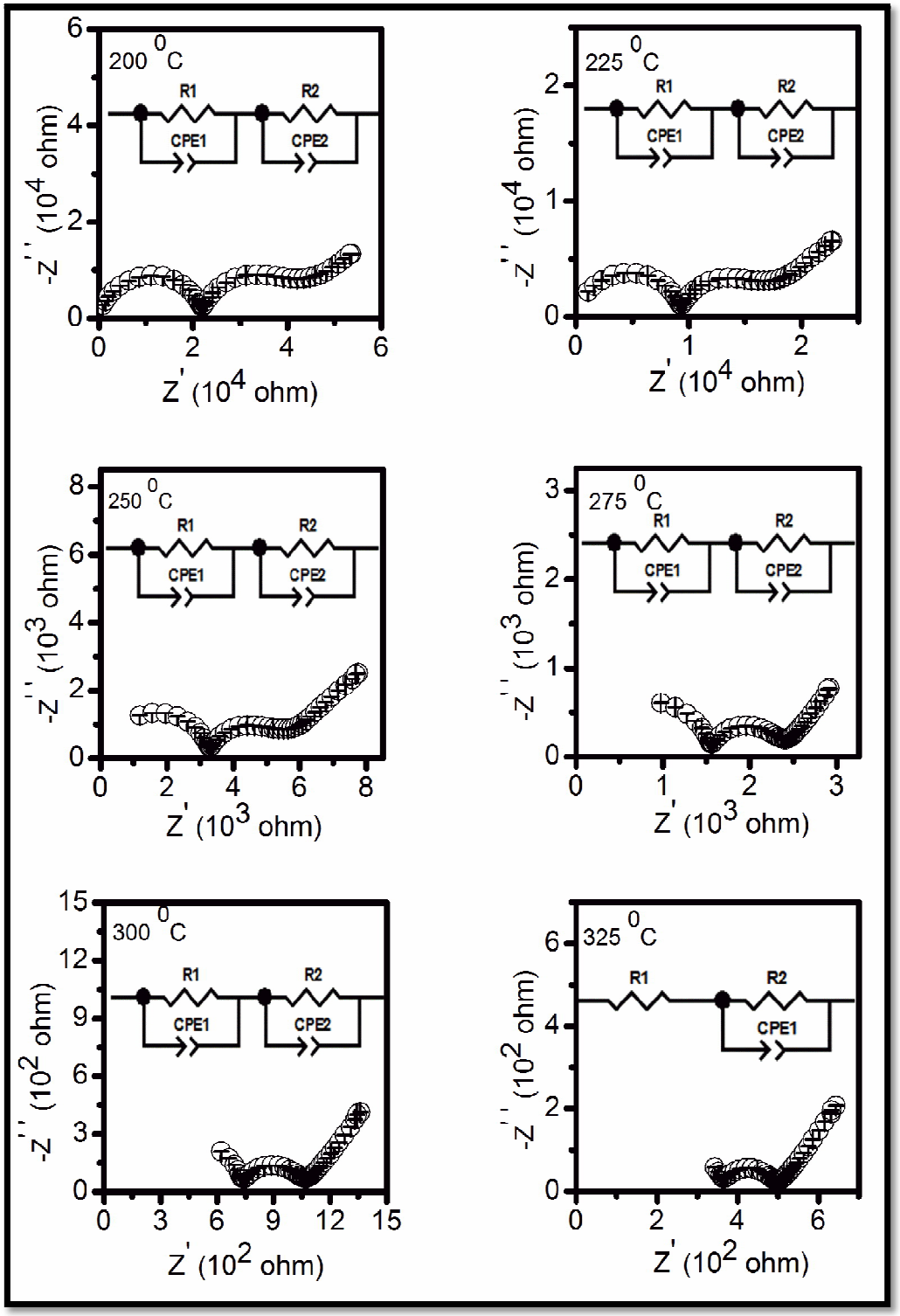

Fig. 4.9 Complex plane impedance plots of the composition CL7S4 at different temperatures

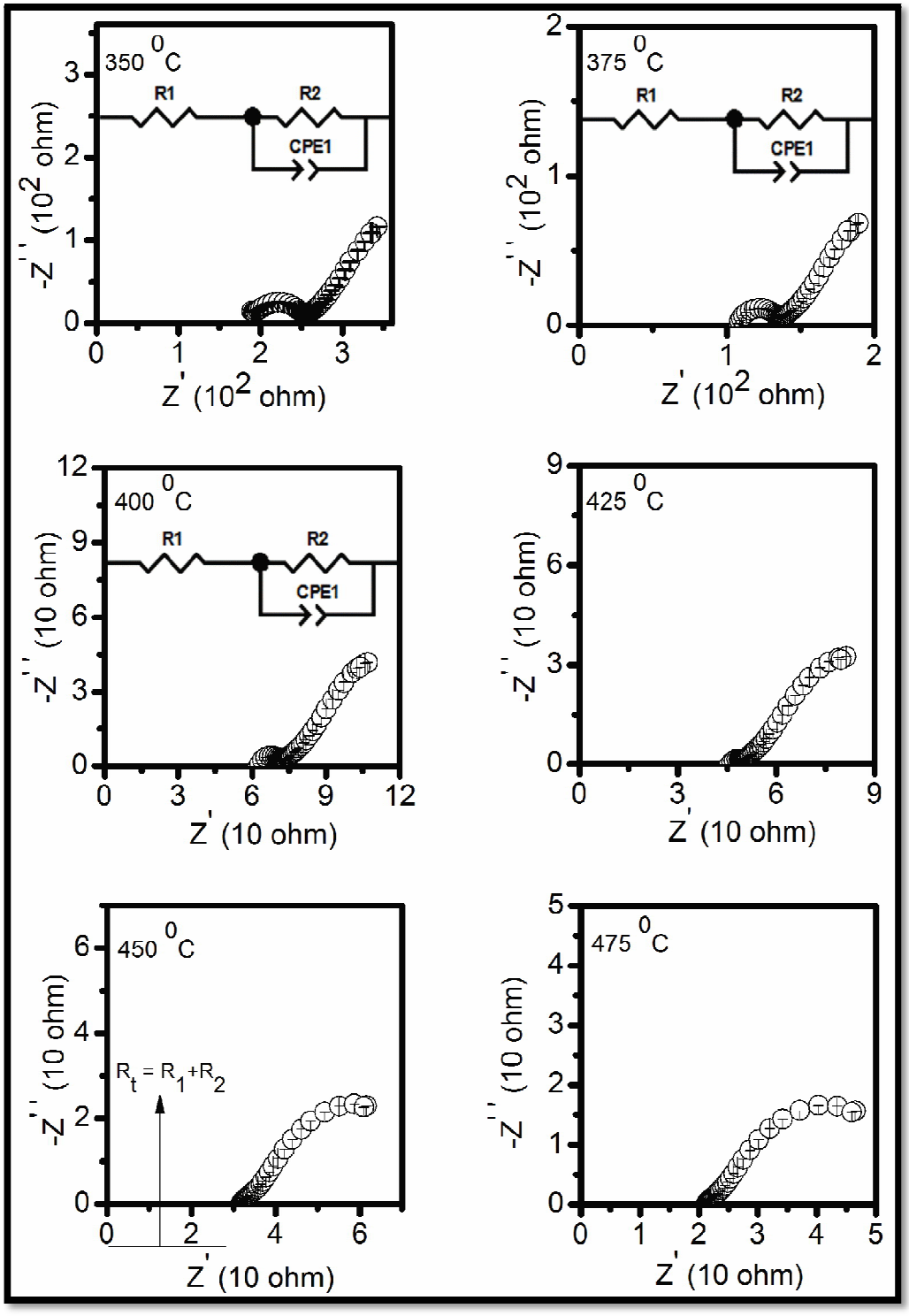

Fig. 4.9 Complex plane impedance plots of the composition CL7S4 at different temperatures

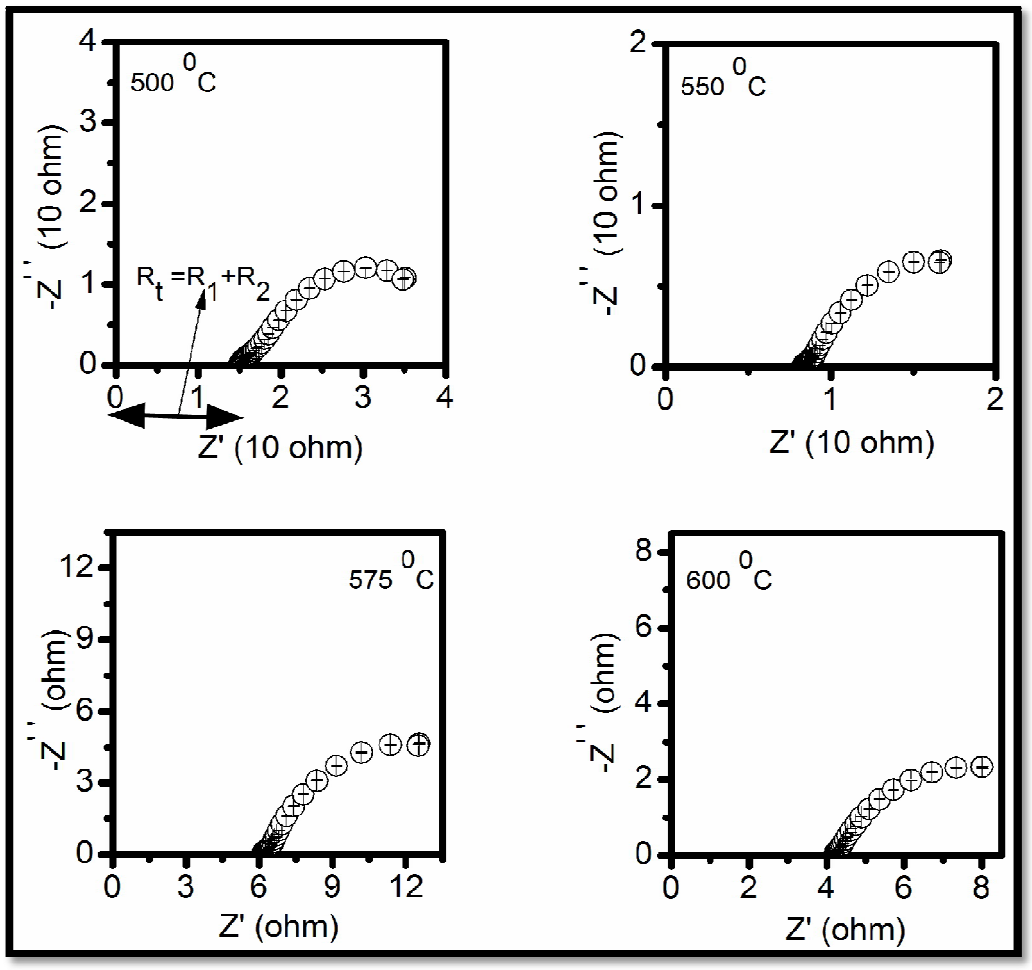

Fig. 4.9 Complex plane impedance plots of the composition CL7S4 at different temperatures

The arc due to the grains disappears above 275 ºC and the arc corresponding to the grain boundaries disappears above 400 ºC. At higher temperatures, only the low frequency arc is observed. For the composition CL3S6, three arcs in the high, intermediate and low frequency range have been observed in the temperature range 200-275 ºC. The arc passing from the origin is ascribed to the polarization of grains and a second arc which follows the earlier one corresponds to the grain boundaries. The arc due to grains and grain boundaries disappear above 275 and 450 ºC respectively. For temperature > 450 ºC, the intercept of the arc on the high frequency side with $Z^{'}$ axis gives the total resistance.

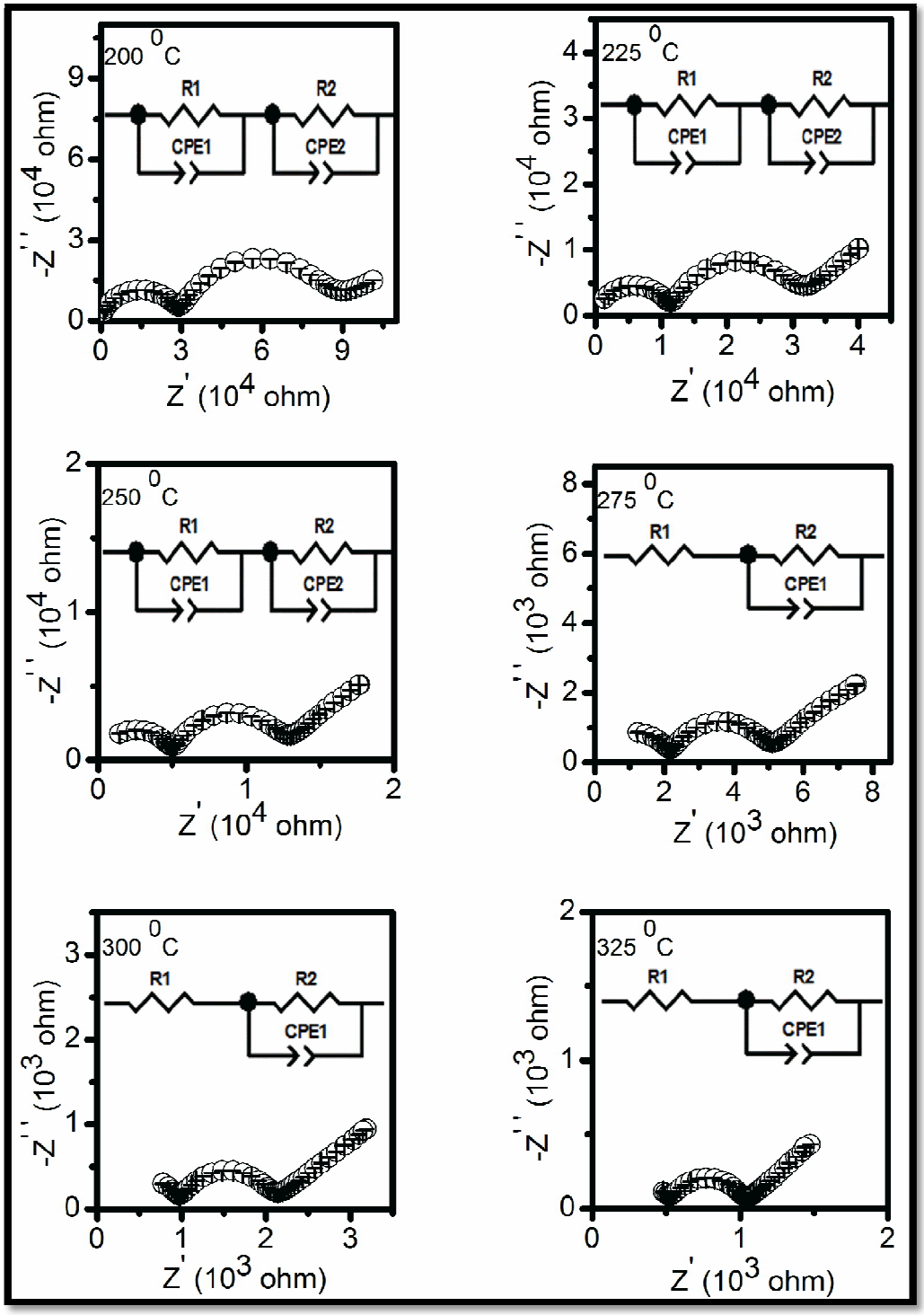

Fig. 4.10 Complex plane impedance plots of the composition CL3S6 at different temperatures

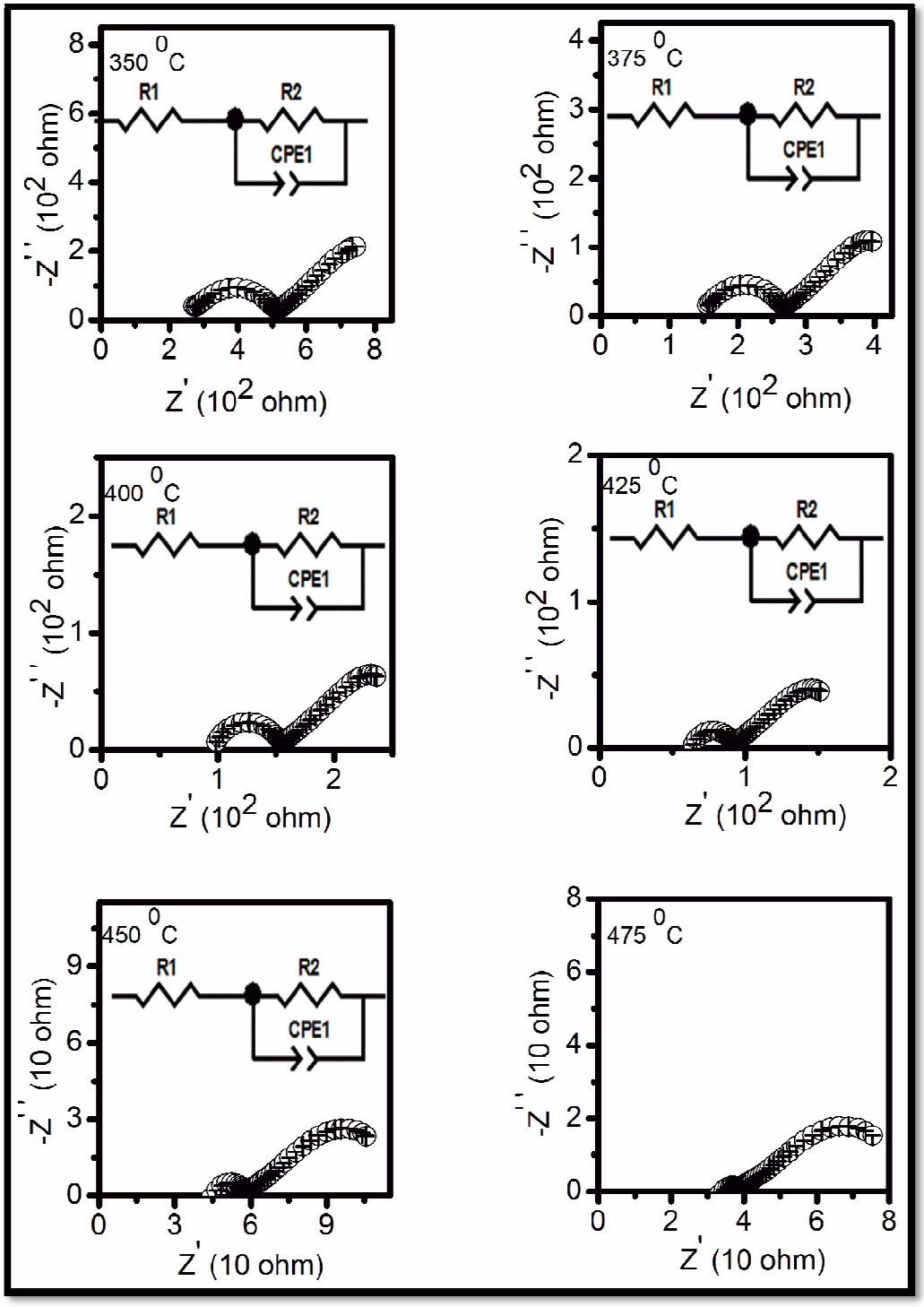

Fig. 4.10 Complex plane impedance plots of the composition CL3S6 at different temperatures

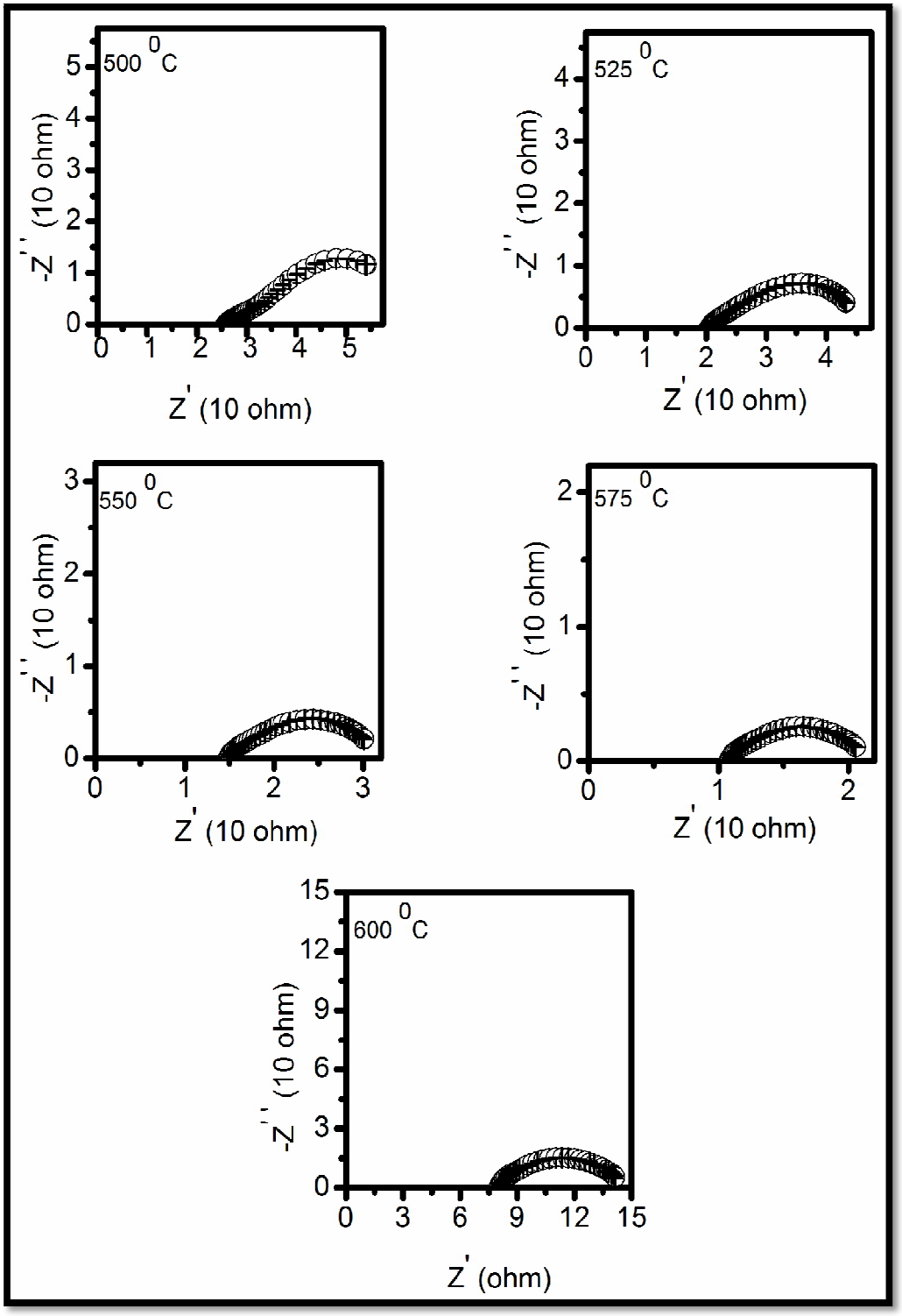

Fig. 4.10 Complex plane impedance plots of the composition CL3S6 at different temperatures

Addition of trivalent or divalent cations to ceria produces oxygen vacancies responsible for ionic conduction in these oxides [Steele (2009); Trejo et al. (2007); Ciotera et al. (2009)] as given below in the Eq[ns]. 4.11 and 4.12.

$$La_2O_3 \xrightarrow{2CeO_2} 2La'_{Ce} + 3O_O + V_O^{\bullet\bullet} \quad (4.9)$$

$$SrO \xrightarrow{CeO_2} Sr''_{Ce} + O_O + V_O^{\bullet\bullet} \quad (4.10)$$

Arrhenius plots for conductivity of the bulk, grain boundaries and total conductivity are shown in Fig. 4.12. It is noted from Fig. 4.12 that Sr^{2+} co-doped samples have higher bulk conductivity, σ_g than that of the singly La doped ceria. σ_g increases with increasing concentration of strontium (y) up to 4 mol%. For higher concentration of Sr^{2+} (y > 0.04) it decreases. Dissolution of Sr^{2+} ions in lanthanum-doped ceria sample will produce a higher association enthalpy for oxygen vacancies and hence lower conductivity [Ciotera et al. (2009)].

Conductivity of the grain boundaries, σ^*_{gb} is calculated using the following formula:

$$\sigma^*_{gb} = \frac{L}{S \times R} \times \frac{\delta_{gb}}{d_g} \quad (4.13)$$

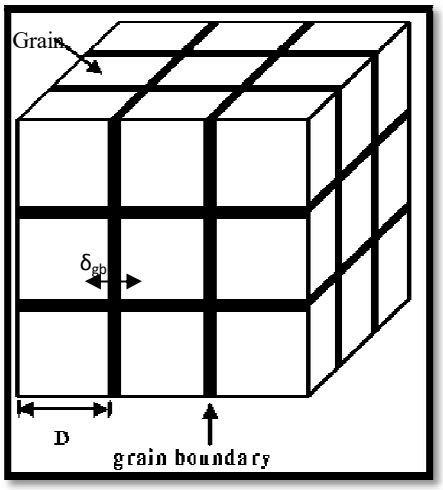

Fig. 4.11 Brick layer model of polycrystalline material [http//www.wikipedia.com

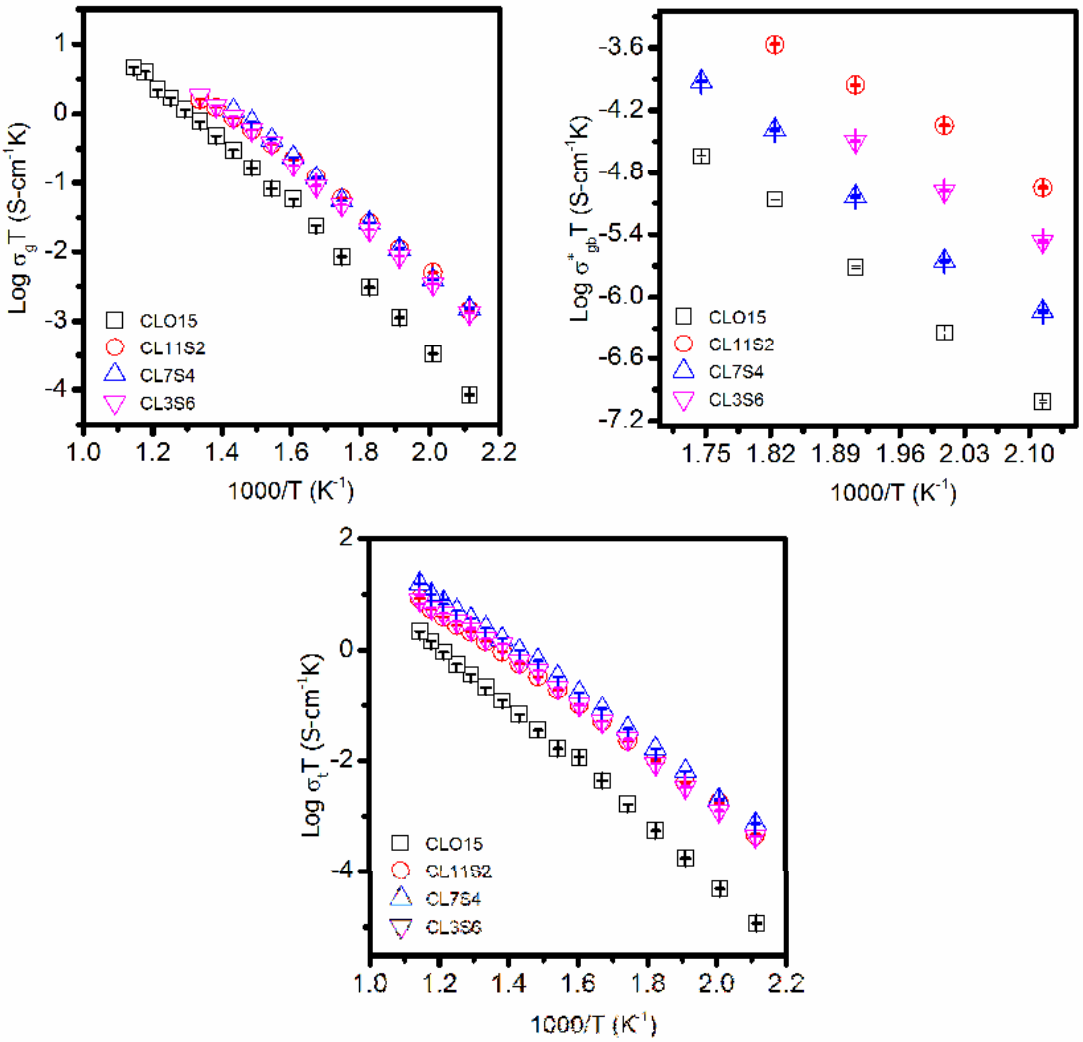

Fig. 4.12 Arrhenius plots of all the compositions for the grain, grain boundaries and total ionic conductivity in the system $Ce_{1-x-y}La_xSr_yO_{2-\delta}$

where, the ratio $\frac{\delta_{gb}}{d_g}$ is the aspect ratio i.e. ratio of the thickness of the grain boundaries (δ_{gb}) to the average grain size (d_g). This ratio was calculated by using brick layer model [Christie et al. (1996)]. This model correlates the electrical properties of the sample to the microstructure and assumes that polycrystalline material consists of cubic grains of length d_g, separated by the flat grain boundaries of thickness δ_{gb} where $\delta_{gb} << d_g$ (Fig. 4.11). The ratio $\frac{\delta_{gb}}{d_g}$ is given as:

$$\frac{\delta_{gb}}{d_g} = \frac{\epsilon_{gb}}{\epsilon_g} \times \frac{CPE1}{CPE2} \qquad (4.14)$$

where, ε_g, ε_{gb}, CPE1 and CPE2 are permittivity of the grains, grain boundaries, capacitance of the grains and grain boundaries respectively. By assuming that $\varepsilon_g = \varepsilon_{gb}$, Eq^n.4.13 is expressed as:

$$\sigma_{gb}^{*} = \frac{CPE1}{CPE2} \times \sigma_{gb} \qquad (4.15)$$

where, σ_{gb} is the apparent grain boundaries conductivity. Value of σ_{gb}^{*} of co-doped samples is more than that of CLO15. This may be due to scavenging effect of Sr^{2+}. To confirm the scavenging effect of strontium, the influence of the grain boundaries conductivity on the total conductivity is evaluated through the blocking factor (α_R) [defined in Chapter 1]. The blocking factor is the minimum for the sample CL7S4 (0.21). For CLO15 its value is 0.90. This confirms that strontium is an effective grain boundaries scavenger.

It is noted from Fig. 4.12 that the sample which has high bulk and total ionic conductivity does not show high grain boundaries conductivity. Grain boundaries conductivity depends on the aspect ratio (ratio, $\frac{\delta_{gb}}{d_g}$). Samples with high aspect ratio exhibits higher grain boundaries conductivity. Values of the aspect ratio of the compositions, CLO15, CL11S2, CL7S4 and CL3S6 are 6.20×10^{-4}, 1.68×10^{-2}, 6.64×10^{-4} and 5.52×10^{-3} respectively. Total conductivity of all the co-doped samples is higher than that of singly La doped sample. The values of total conductivity, configurational entropy (S) and the activation energy of conduction are given in Table.4.2.

It is noted from Table. 4.2 that enhancement in the conductivity do not follow the criteria of configurational entropy in the system $Ce_{1-x-y}La_xSr_yO_{2-\{x/2+y\}}$. Therefore, it is concluded that configurational entropy is not a major factor to optimize the conductivity in co-doped ceria systems. Composition $Ce_{0.89}La_{0.07}Sr_{0.04}O_{1.92}$ shows the highest total conductivity among all the samples.

The ionic conductivity of CL7S4 (4.75×10^{-3} S/cm) is one order of magnitude is more than that of CLO15 (4.84×10^{-4} S/cm) at 500 °C. It suggests that co-doping by an optimum ratio of La^{3+} and Sr^{2+} enhances the conductivity.

Ionic conductivity of $Ce_{0.89}La_{0.07}Sr_{0.04}O_{1.925}$ at 600 °C is 1.78×10^{-2} S/cm. This value is slightly more than that of $Ce_{0.8}Sm_{0.2}O_{1.90}$ (1.20×10^{-2} S/cm) [Balazas et al. (1995)] and $Ce_{0.8}Gd_{0.2}O_{1.90}$ (1.29×10^{-2} S/cm) [Fu et al. (2010)] at the same temperature.

Table. 4.2 Total conductivity (at 600 ºC), activation energy of grains (E_g), grain boundaries (E_{gb}) and total (E_t) of various compositions of the system $Ce_{1-x-y}La_xSr_yO_{2-\{x/2+y\}}$

S. No.	x & y	Sample code	σ_t at 600 °C (S/cm)	S (J/mol K)	E_g (eV)	E_{gb} (eV)	E_t (eV)
1.	0.15 & 0.0	CLO15	2.50×10^{-3}	3.50	0.89	0.98	0.97
2.	0.11 & 0.02	CL11S2	9.75×10^{-3}	3.67	0.79	0.98	0.88
3.	0.07 & 0.04	CL7S4	1.78×10^{-2}	3.50	0.85	1.11	0.91
4.	0.03 & 0.06	CL3S6	9.22×10^{-3}	3.00	0.83	1.05	0.92

In this study, partial substitution of Sr^{2+} in place of La^{3+} causes three effects in the system, $Ce_{1-x-y}La_xSr_yO_{2-\{x/2+y\}}$. The number of $[La'_{Ce}\text{-}V_O^{\bullet\bullet}]^{\bullet}$ pairs decreases as twice the number of Sr^{2+} ions added. This decreases the total number of associated defect pairs leading to enhancement of the ionic conductivity. Due to scavenging effect of Sr, grain boundaries as well as the total conductivity increases. Replacement of La^{3+} by Sr^{2+} increases the lattice strain [Kim (1989)] due to larger size of Sr^{2+} ion (1.26 Á) as compared to La^{3+} ion (1.16 Á). This causes the increase in association enthalpy of dopant-vacancy pairs $[Sr''_{Ce}\text{-}V_O^{\bullet\bullet}]^{\times}$ [Butler et al. (1983); Kilner (1983)]. Consequently activation energy increases and hence ionic conductivity decreases. For compositions with $y \leq 0.04$, the first two factors seem to dominate leading to an increase in the ionic conductivity. For $y > 0.04$, the later two factors may start dominating causing a decrease in the ionic conductivity. $y = 0.04$ seems to be an optimum value for molar

concentration of Sr^{2+} which gives the maximum conductivity. Ionic conductivity increases also due to scavenging effect of strontium. Since conductivity of the composition, CL7S4 is comparable to the highest conductivity reported for SDC and GDC, use of this material as a solid electrolyte for IT-SOFCs will reduce the cost.

4.1.3. Conclusions

- Samples of ceria co-doped with La and Sr, $Ce_{1-x-y}La_xSr_yO_{2-\{x/2+y\}}$ {(x= 0.15, y=0), (x=0.11, y=0.02), (x=0.07, y=0.04) and (x=0.03, y=0.06)} having equal molar concentration of oxygen vacancies have been prepared successfully by citrate-nitrate auto-combustion method.
- All the compositions show single phase formation. Density obtained by sintering at 1350 °C is more than 95% of the theoretical value.
- By assuming average radius of oxygen vacancies formed due to substitution of divalent and trivalent cations in ceria, theoretical values of lattice parameter matches closely with the experimental values.
- Sr^{2+} acts as a good grain boundaries scavenger causing an increase in the conductivity of the grain boundaries.
- $Ce_{0.89}La_{0.07}Sr_{0.04}O_{1.925}$ shows higher conductivity than that of ceria doped with lanthanum only having the same number of oxygen vacancies. This is also higher than the maximum value reported in the system, SDC and GDC.

4.2. Nanocomposites of La and Sr Co-Doped Ceria (CL7S4)

4.2.1 Introduction

A large number of efforts have been made for the improvement of ionic conductivity of solid electrolytes including zirconia-based oxides, bismuth-based oxides, lanthanum gallate-based oxides, and the ceria-based oxides [Kharton et al. (2004); Ishihara et al. (2006); Sammes et al. (1999); Minh (1995)]. Among these electrolytes, yttria stabilized zirconia (YSZ) exhibits high ionic conductivity. But its high working temperature ~ 1000 ºC puts lot of constraints on using expensive materials for various

components of the cell/cell stacks. Gadolinium (GDC) and samarium (SDC) doped ceria show much higher ionic conductivity than YSZ in the intermediate temperature range. But Gd and Sm are very costly. Doped ceria electrolytes show mixed ionic and electronic conductivity due to conversion of Ce^{4+} to Ce^{3+} in the reducing atmosphere. This leads to a significant decrease in power output and efficiency of the cells [Dudek (2008); Tadokoro et al. (2007)].

Shiqiang et al. (2007) suggested the idea of composite i.e. introducing a liquid phase at the grain boundaries/interfaces forming the composite electrolyte may improve the ionic conductivity. Composite electrolyte contains two phases, one based on crystalline ceria and other is of amorphous salts. Salts exist in a molten state e.g. eutectic mixture of Li_2CO_3 and Na_2CO_3 above 500 ºC. It has been demonstrated that the interfaces provide more conducting channels for ions transport. The interface regions have no structural limit for creation of mobile ions [Zhu et al. (2008)]. This implies that interface regions have larger concentration of mobile ions than that in the bulk.

Electric field distribution in the interfaces between two phases is a key to realize the interface ionic conduction. This allows ions to move on the surfaces or interfaces through high conducting path ways. It has been reported by Huang et al. (2006) that O^{2-} ions could conduct through the bulk and interface region formed between the ceria and the carbonate phases. H^+ ion conduction also occurs via HCO_3^- in H_2/O_2 fuel environment during the cell operation. M^+ cations (e.g. Li^+, Na^+) and CO_3^{2-} ions also contribute to the conductivity above the melting temperature [Liu et al. (2010)]. In the molten carbonate fuel cells (MCFCs), the electrolyte is the eutectic mixture of Li_2CO_3 and Na_2CO_3 [$(Li\text{-}Na)_2CO_3$] retained by $LiAlO_2$ insulating solid phase. The electrolyte must contain above 40 wt% of carbonates and operate at 650 °C [Zhu et al. (2006)]. In ceria/carbonate composite, the carbonate content was used up to 40 wt% to avoid deformation of the pellets [Huang et al. (2007)]. Among the series of composite electrolytes, doped ceria-carbonate composites show a better performance than the other ceria-salt composite electrolytes [Zhu et al. (2003); Wang

et al. (2008); Di et al. (2010); Fan et al. (2011); Wang et al. (2011); Huang et al. (2005); Lapa et al. (2010)]. According to previous reported results, it has been found that co-doping enhances the electrical conductivity of ceria based composite electrolytes [Liu et al. (2010)]. Therefore by using co-doped ceria/carbonates composites conductivity may further improve at lower temperatures.

It has been found from the above results (section 1) that the composition $Ce_{0.89}La_{0.07}Sr_{0.04}O_{1.925}$ (CL7S4) shows the highest ionic conductivity of all the compositions. A few compositions of CL7S4/(Li-Na)$_2CO_3$ nanocomposite have been prepared and characterized by studying thermal behavior, crystal structure, coefficient of thermal expansion, microstructure, elemental analysis and impedance spectroscopy.

4.2.2 Results and discussion

(a) Thermal analysis

DTA plots of all the composites are shown in Fig. 4.13. Two endothermic peaks have been observed in the DTA plot for all the samples. One is observed in the temperature range 100-150 °C. This is due to evaporation of adsorbed moisture.

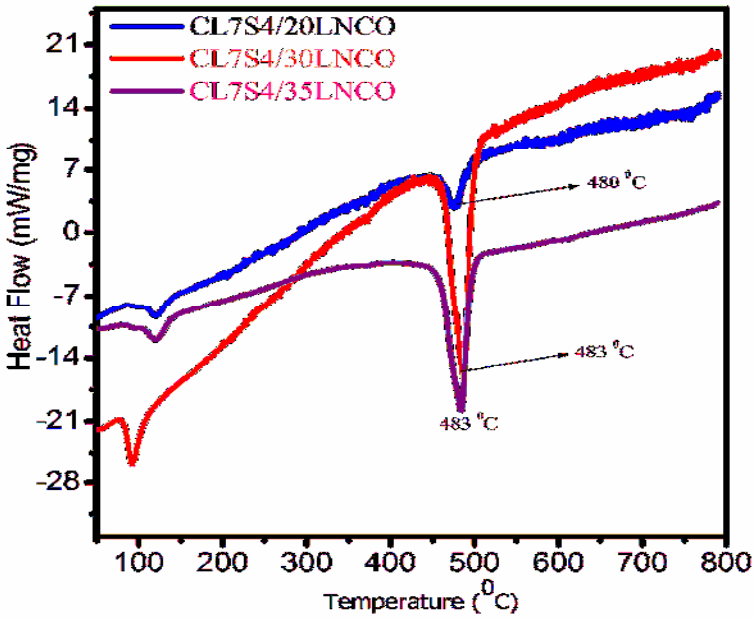

Fig. 4.13 DTA plots of all the CL7S4/LNCO nanocomposite powders

Second endothermic peak has been observed at 480, 484 and 489 ºC for the compositions CL7S4/20LNCO, CL7S4/30LNCO and CL7S4/35LNCO respectively. This corresponds to melting of the eutectic binary mixture of carbonates. Molten $(Li\text{-}Na)_2CO_3$ fills in the interspaces among the ceria particles and increases the density. No endo or exothermic peak is present above 500 °C. Based on these DTA results, the composite samples were calcined at 600 °C for 2 hrs.

(b) Crystal structure and phases

Powder X-ray diffraction patterns of all the milled (uncalcined), calcined and sintered samples are recorded. XRD patterns have been indexed on the basis of fluorite structure similar to ceria using JCPDS file no. 43-1002. Fig. 4.14 shows XRD patterns of all the sintered samples (sintered at 700 ºC) of CL7S4/LNCO nanocomposites along with CL7S4 (sintered at 1350 ºC). No peak due to any secondary phase has been observed in the XRD patterns. Absence of diffraction peaks of carbonates in the XRD patterns shows that carbonates exist as an amorphous phase in the composites.

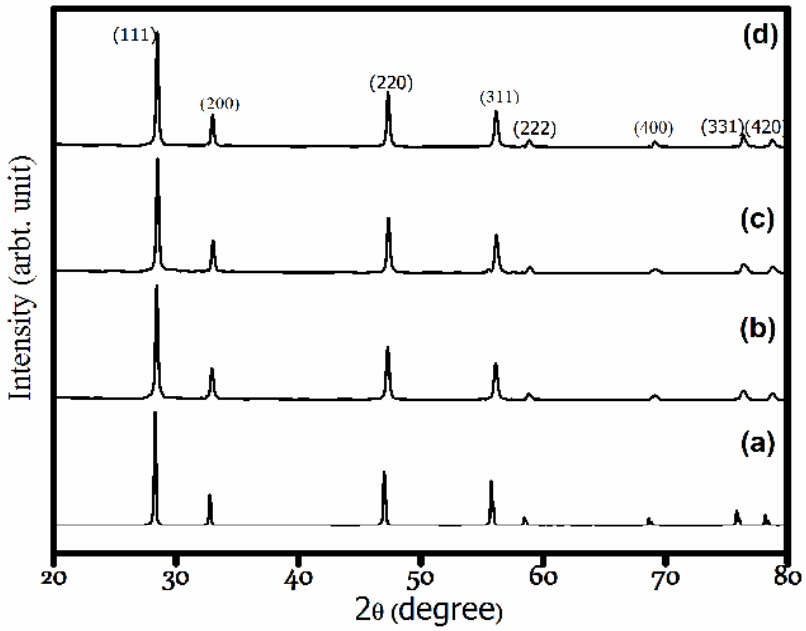

Fig. 4.14 XRD patterns of all the sintered samples: (a) CL7S4/35 LNCO (b) CL7S4/30 LNCO (c) CL7S4/20 LNCO and (d) CL7S4

XRD patterns of the milled powder are the same as that of the calcined and sintered samples except that diffraction lines are broad in the case of milled samples. Average crystallite size of the milled composites powders (uncalcined) has been found to be in the range of 15-20 nm. Nanosized particles lead to more interaction among the particles of the two phases due to large surface area which tends to large interface region.

Density of the sintered composite pellets is found to be in the range 82-85% of the theoretical value. Value of experimental density is low because sintering was carried out at low temperature of 700 ºC. Composites, however, can still be used as an electrolyte because carbonates melt at the working temperature and serve as seals to avoid crossover of the gases [Di et al. (2010)].

(c) Microstructure

Micrographs of the composition, CL7S4 (sintered at 1350 °C) and all the sintered composite samples are shown in Figs. 4.15 (a)-(d). It is seen from Figs. 4.15 (b)-(d) that CL7S4 grains are surrounded by the amorphous carbonate phase. As carbonate content increases, a continuous carbonate layer is formed. Due to the presence of large pores between the ceramic grains, percolation of the carbonate phase is obvious. It is noted from micrographs that average grain size of the composites is less than 100 nm. These micrographs show that the interface between ceria and carbonates phase provides more paths for ionic conduction. Fig. 4.16 shows EDS spectrum of the composition, CL7S4/35LNCO at two different points in the sample. All the constituent elements are present in the expected concentration. It is observed from EDS spectra that both the ceria and carbonates phases are distributed homogeneously. It is noted that Li is not detected by EDS.

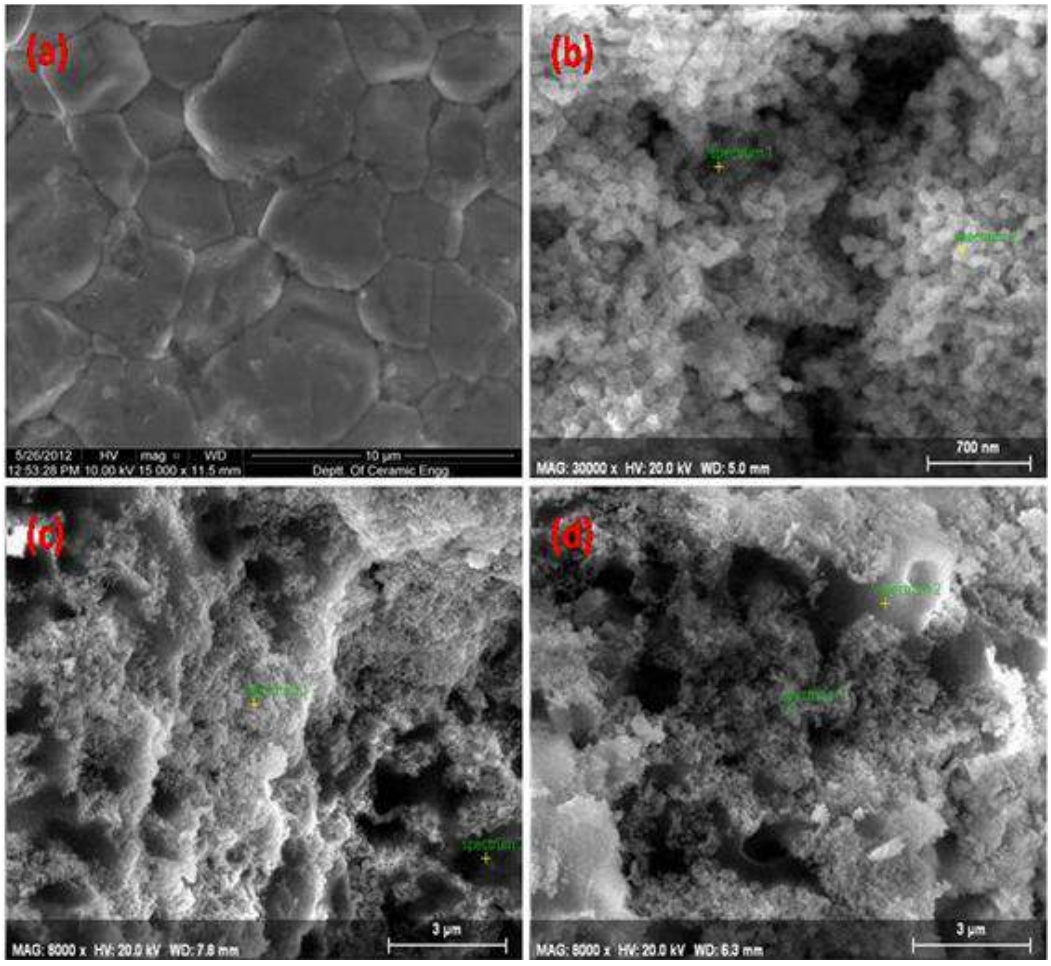

Fig. 4.15 SEM micrograph of the sintered samples of compositions (a) CL7S4: after polishing and thermal etching (b) CL7S4/20 LNCO: fractured surface (c) CL7S4/30 LNCO: fractured surface (d) CL7S4/35 LNCO: fractured surface

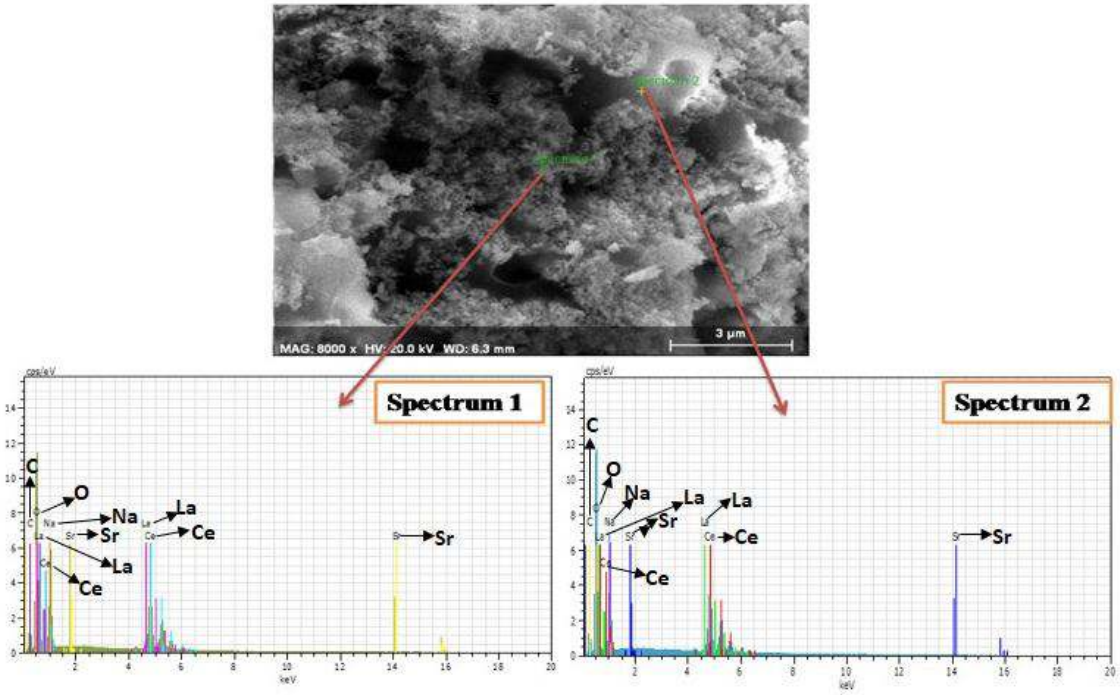

Fig. 4.16 EDS spectrum of the composition CL7S4/35LNCO at two points

(d) Thermal expansion

Plots of thermal expansion of all the composites are shown in Fig. 4.17. It is noted that expansion behavior of all the samples is nonlinear with temperature having an inflection point in the temperature range 723-773 K. Inflection point around 723 K is attributed to the phase transition of carbonate from solid phase to liquid phase. Around 773 K, remaining carbonates melt and fill in the interspaces forming a continuous path. Thermal expansion curve is again linear above 773 K. It is also seen from Fig. 4.17 that below 723 K thermal expansion of the composites increases with increase in carbonates content. Values of thermal expansion coefficient (CTE) are given in Table. 4.3.

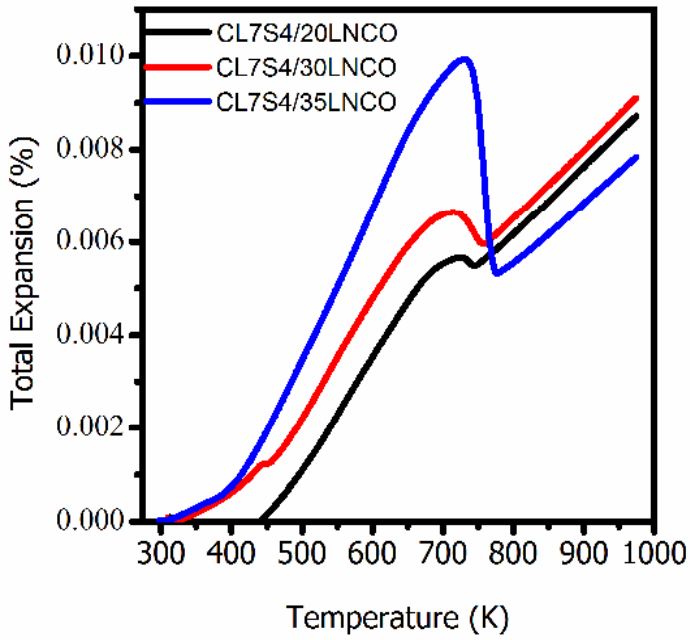

Fig. 4.17 Thermal expansion curves for all the nanocomposites in the system CL7S4/LNCO

Table 4.3 Coefficient of thermal expansion of all the composites

S. No.	Compositions	CTE (K^{-1})
1.	CL7S4/20LNCO	4.8×10^{-6}
2.	CL7S4/30LNCO	5.0×10^{-6}
3.	CL7S4/35LNCO	5.6×10^{-6}

(e) Electrical conductivity

Complex plane impedance plots for all the composites and the pure molten carbonates mixture at different temperatures are shown in Figs. 4.18 to 4.21. In the case of composites, three depressed arcs have been observed at 200 ºC. The high frequency arc corresponds to the contribution of the grains and an intermediate frequency arc is ascribed to the grain boundaries.

A tail in the low frequency region corresponds to the contribution of electrode/electrolyte interface to the total resistance. As temperature increases, relaxation frequency of various polarization processes increases leading to shifting of the arcs toward higher frequency. The arcs of grains and grain boundaries are associated with the capacitances in the pF (10^{-10}-10^{-12}) and nF (10^{-7}-10^{-9}) ranges. These are determined from the relation $2\pi f_{max}RC = 1$, where f_{max} is the frequency at the highest point of the arc and R is the resistance and C is the capacitance of a particular contribution [Hodge et al. (1976)]. Arcs due to grains and grain boundaries disappear around 350 ºC. At higher temperature, only the arc due to electrode polarization is observed. The low frequency arc is large because of the barrier between the ionic conduction in the electrolyte and electronic conduction in the electrode [Wang et al. (2008)]. Above 450 ºC, the electrode arc is associated with a tail which is ascribed to mass transfer process [Di et al. (2010)]. It is clear from this distinct phenomenon that the conduction mechanism in the composite electrolytes is different from the ceria based ceramic electrolyte.

The impedance plots were fitted to an equivalent circuit as shown in the Figs. 4.18-4.20. In the present investigation, only the arcs of grains and the grain boundaries are fitted because the sum of the resistance of the grains and the grain boundaries is equal to the total resistance of the sample. The arc of electrode, therefore, is not fitted. At higher temperatures, total resistance is determined from the intercept on the real axis (Z') on the higher frequency side of the electrode arc.

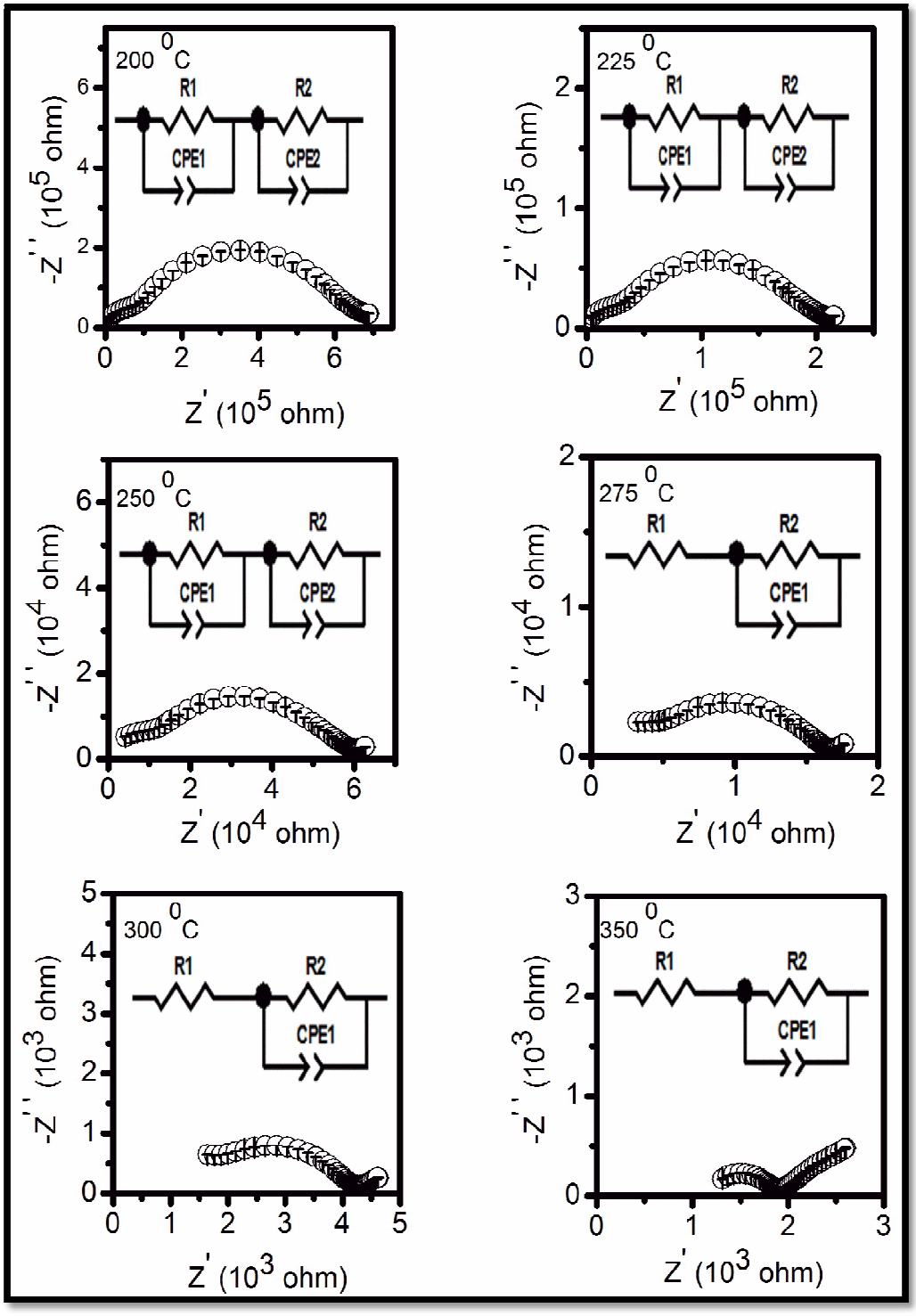

Fig. 4.18 Complex plane impedance plots of the composition CL7S4/20LNCO at different temperatures

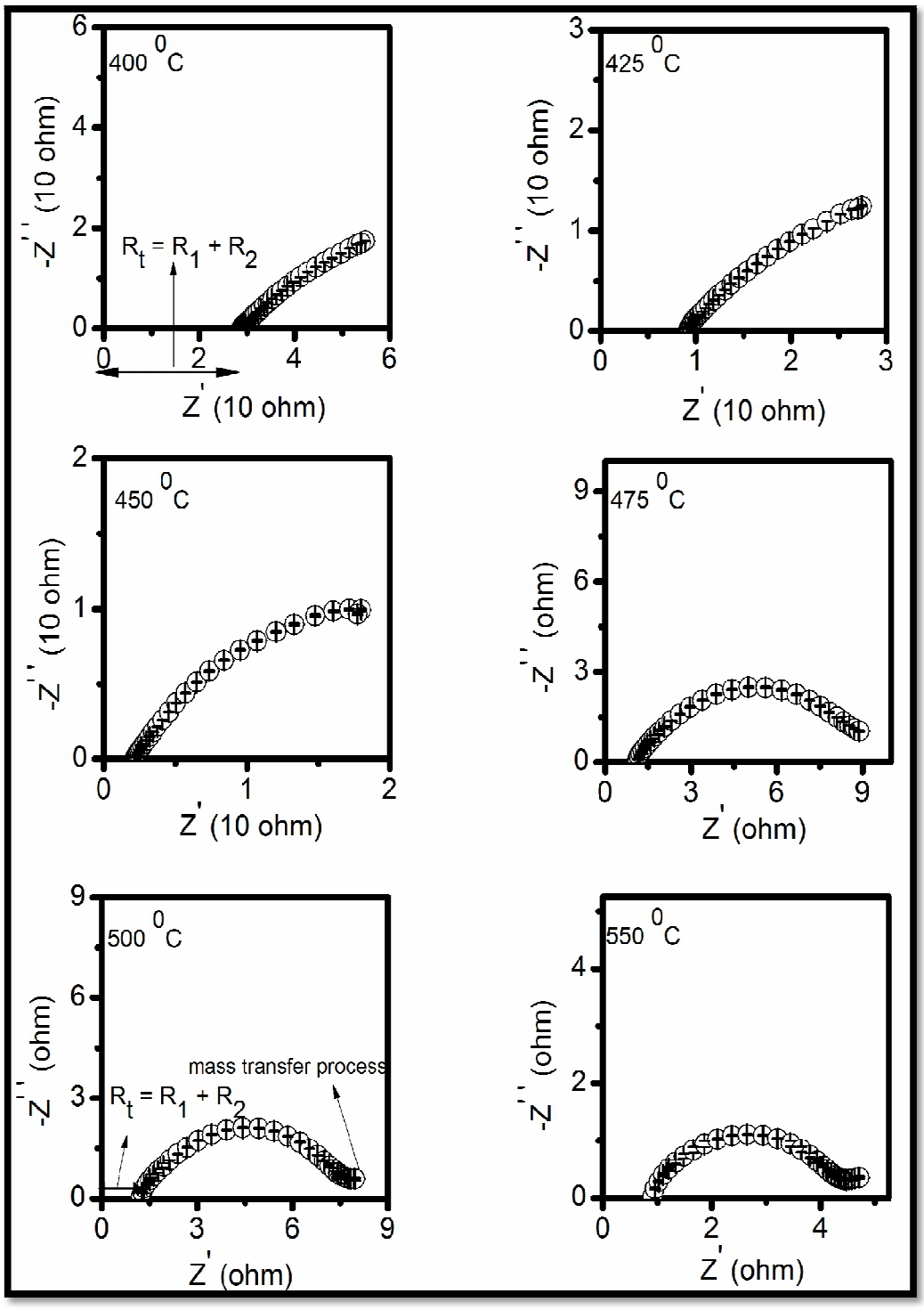

Fig. 4.18 Complex plane impedance plots of the composition CL7S4/20LNCO at different temperatures

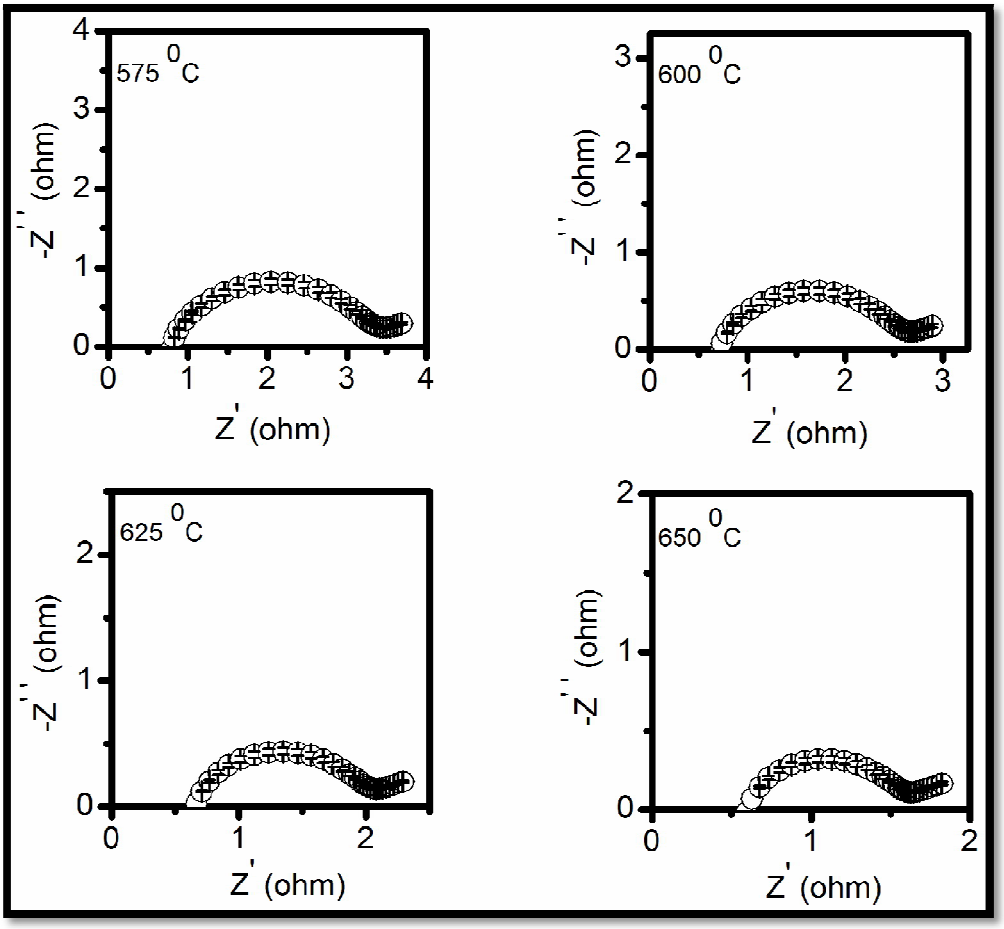

Fig. 4.18 Complex plane impedance plots of the composition CL7S4/20LNCO at different temperatures

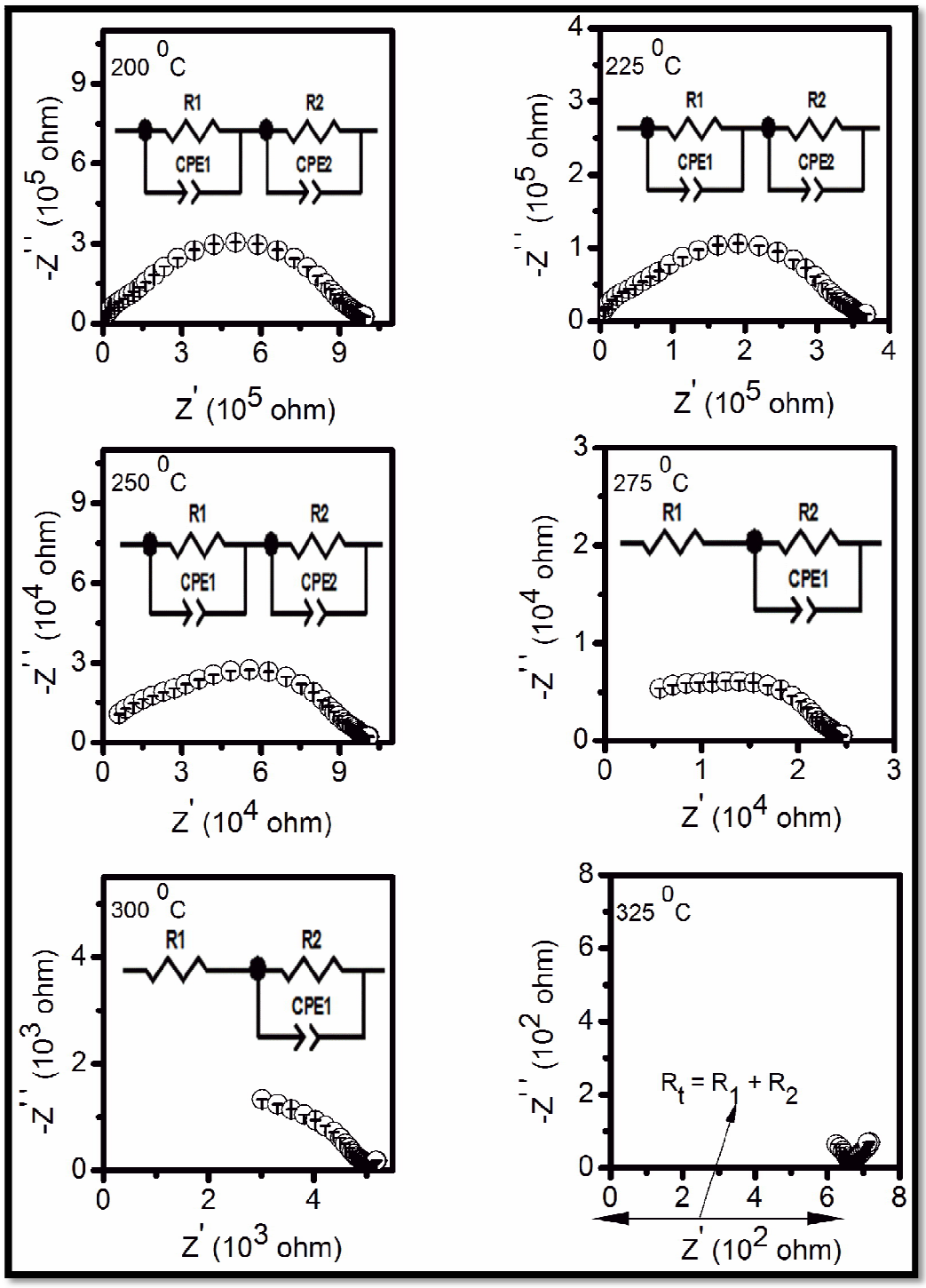

Fig. 4.19 Complex plane impedance plots of the composition CL7S4/30LNCO at different temperatures

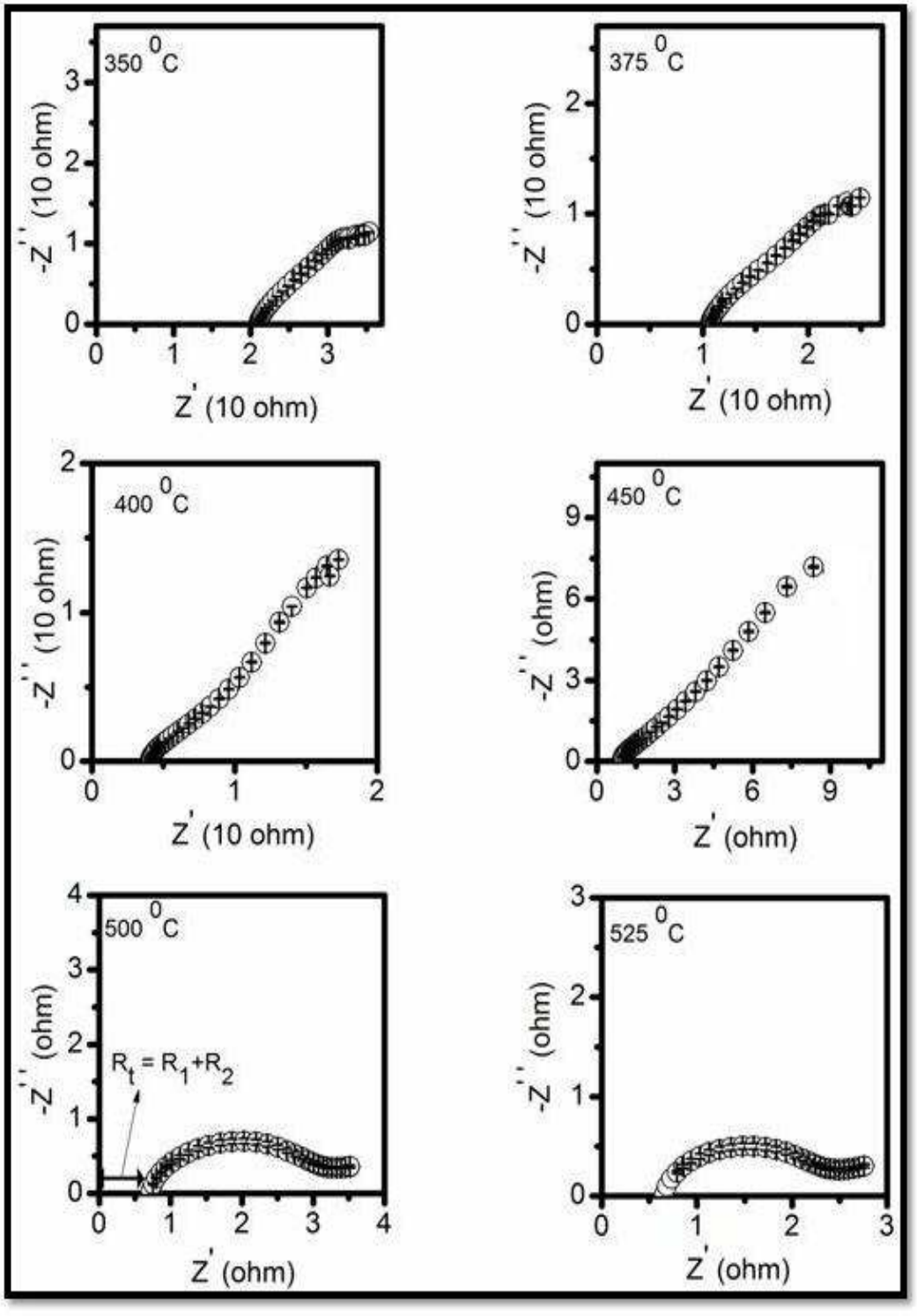

Fig. 4.19 Complex plane impedance plots of the composition CL7S4/30LNCO at different temperatures

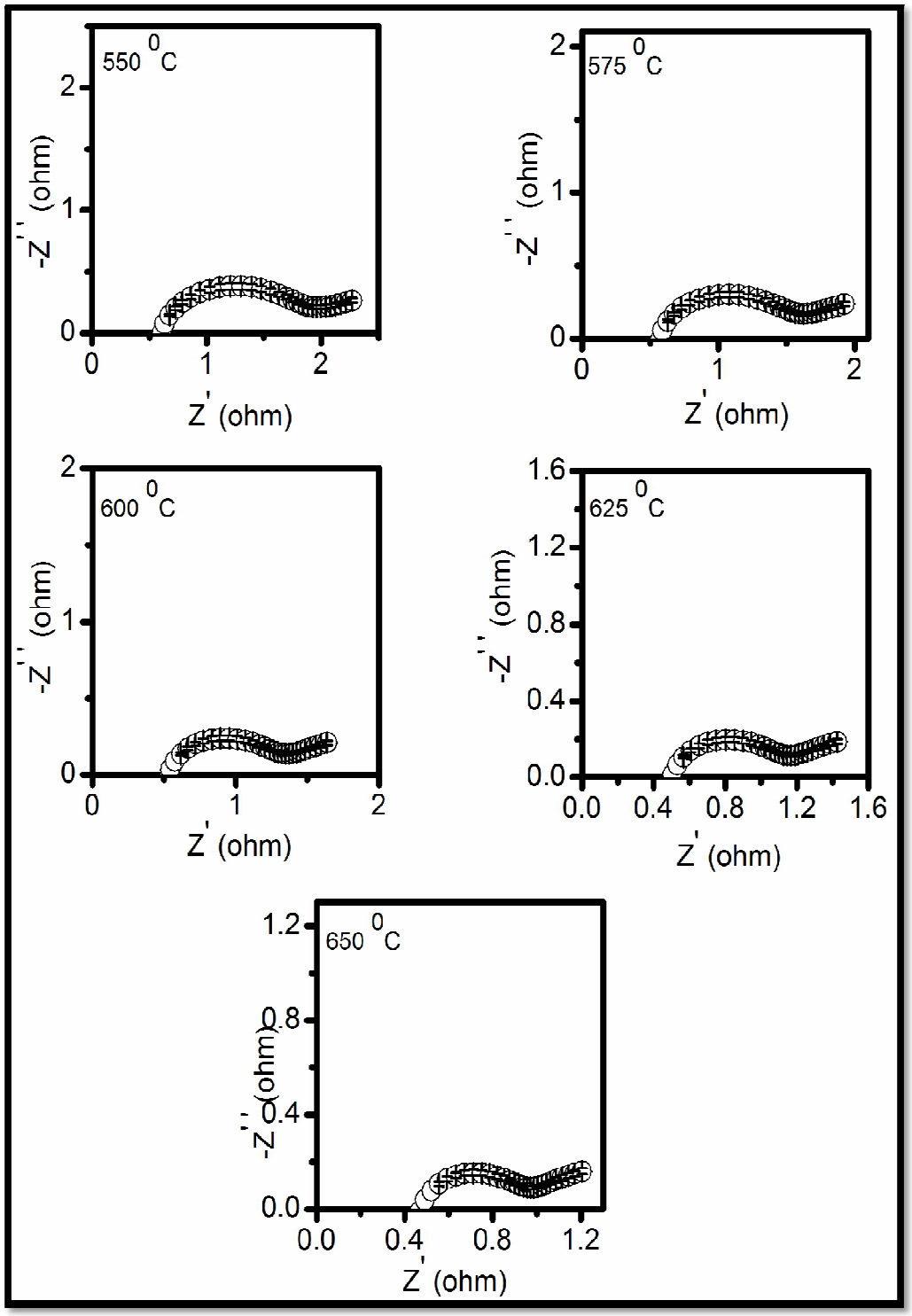

Fig. 4.19 Complex plane impedance plots of the composition CL7S4/30LNCO at different temperatures

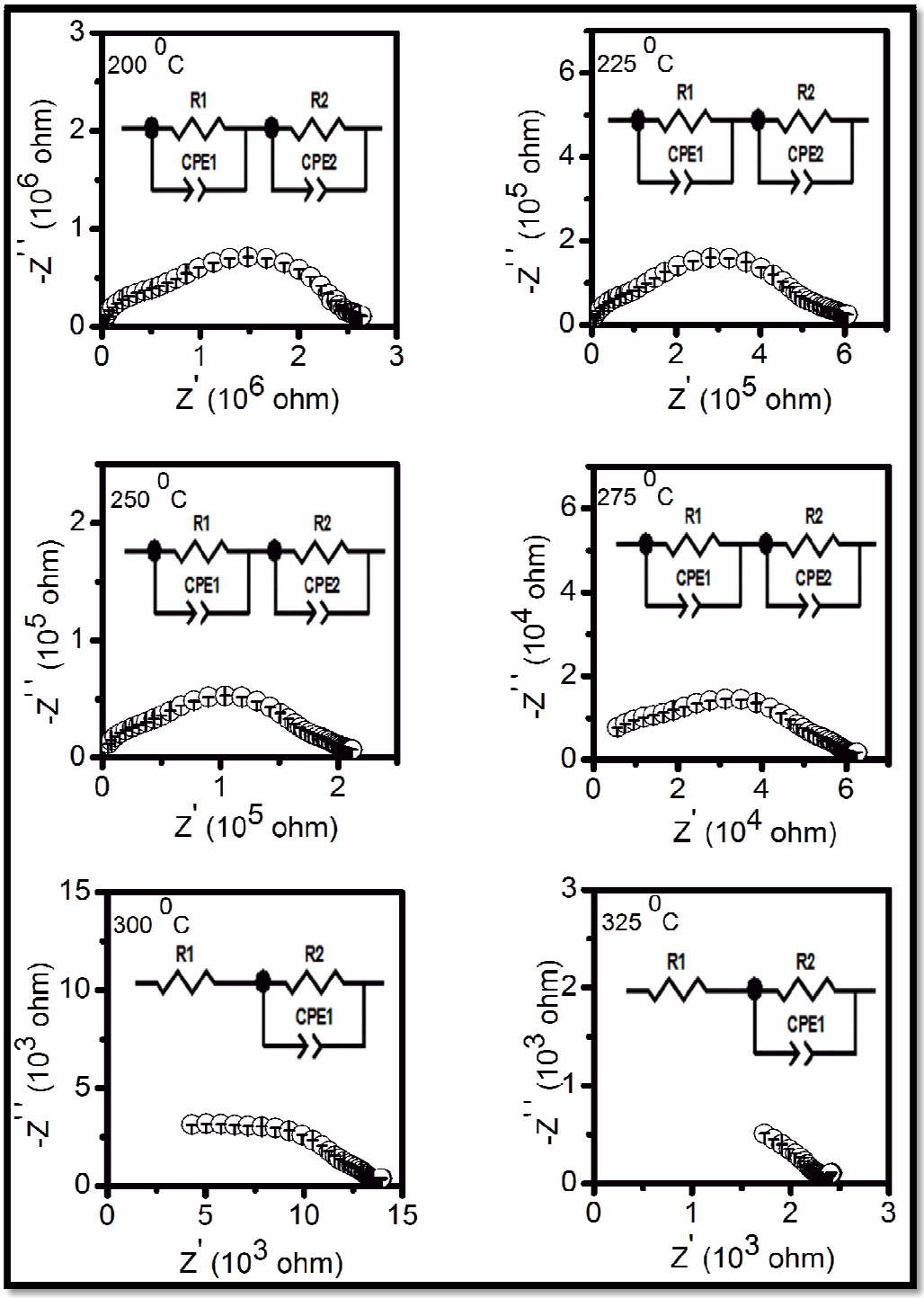

Fig. 4.20 Complex plane impedance plots of the composition CL7S4/35LNCO at different temperatures

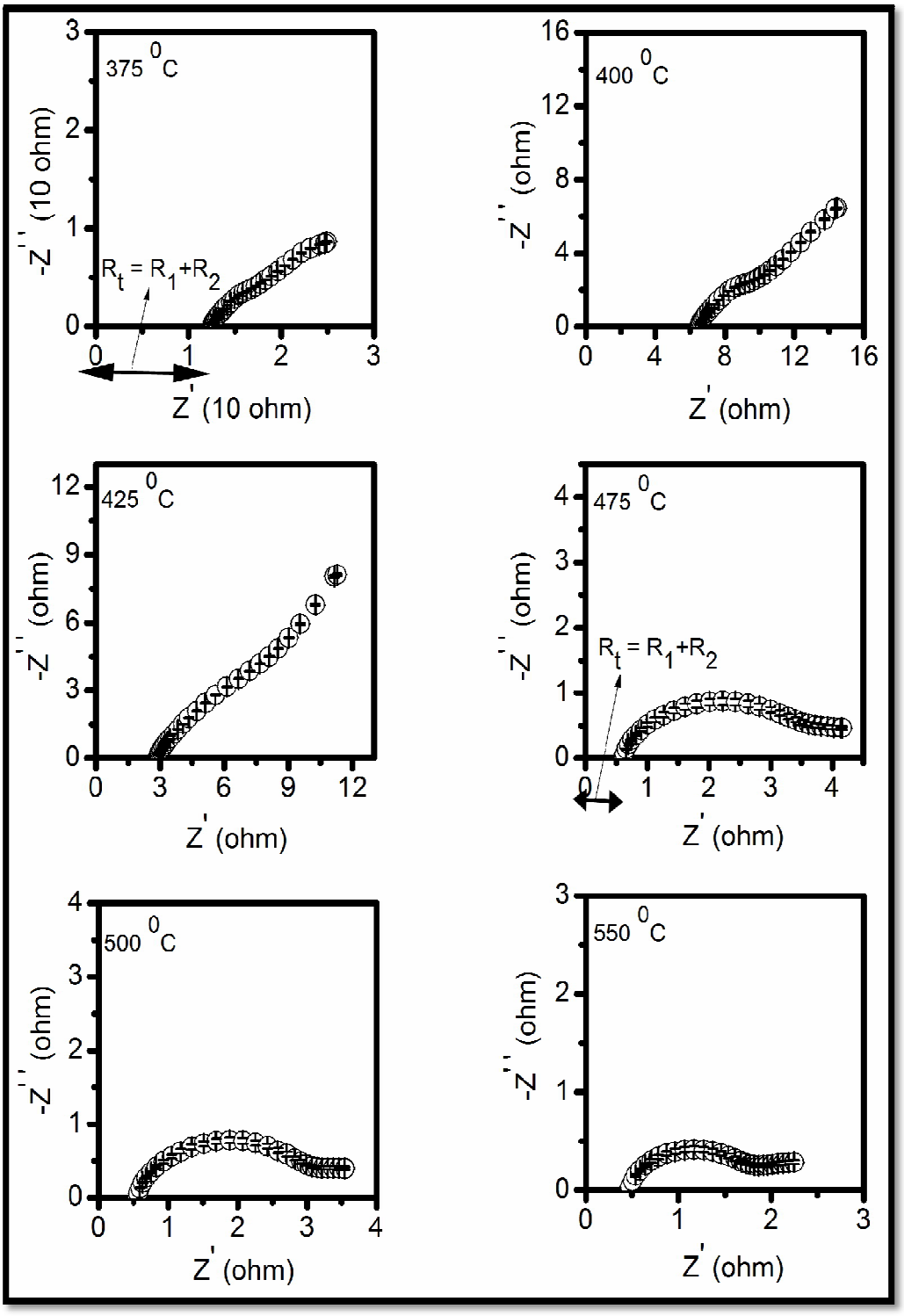

Fig. 4.20 Complex plane impedance plots of the composition CL7S4/35LNCO at different temperatures

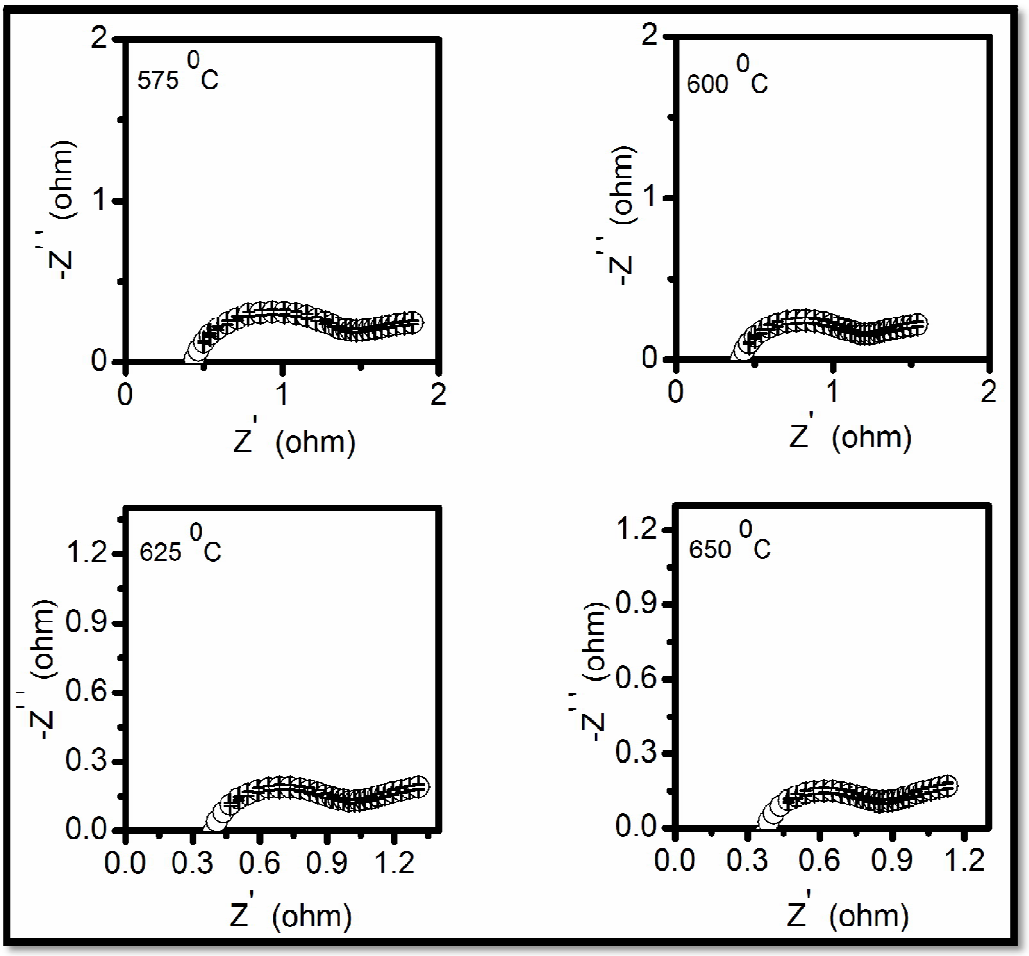

Fig. 4.20 Complex plane impedance plots of the composition CL7S4/35LNCO at different temperatures

In the case of pure carbonate mixture (Fig. 4.21) only one high frequency arc passing from the origin has been observed in the temperature range 200-400 ºC. It is noted from these plots that grain and grain boundaries arcs are not distinct. Above 400 ºC, only the arc due to electrode has been observed. Below 400 ºC, impedance plots are fitted to an equivalent circuit consisting of a single R_1-CPE1 element connected in parallel. Only the arc of the grains is fitted to determine the total resistance of the sample. The intercept on the real axis at higher frequency side has been taken as the total resistance when the high frequency arc disappears.

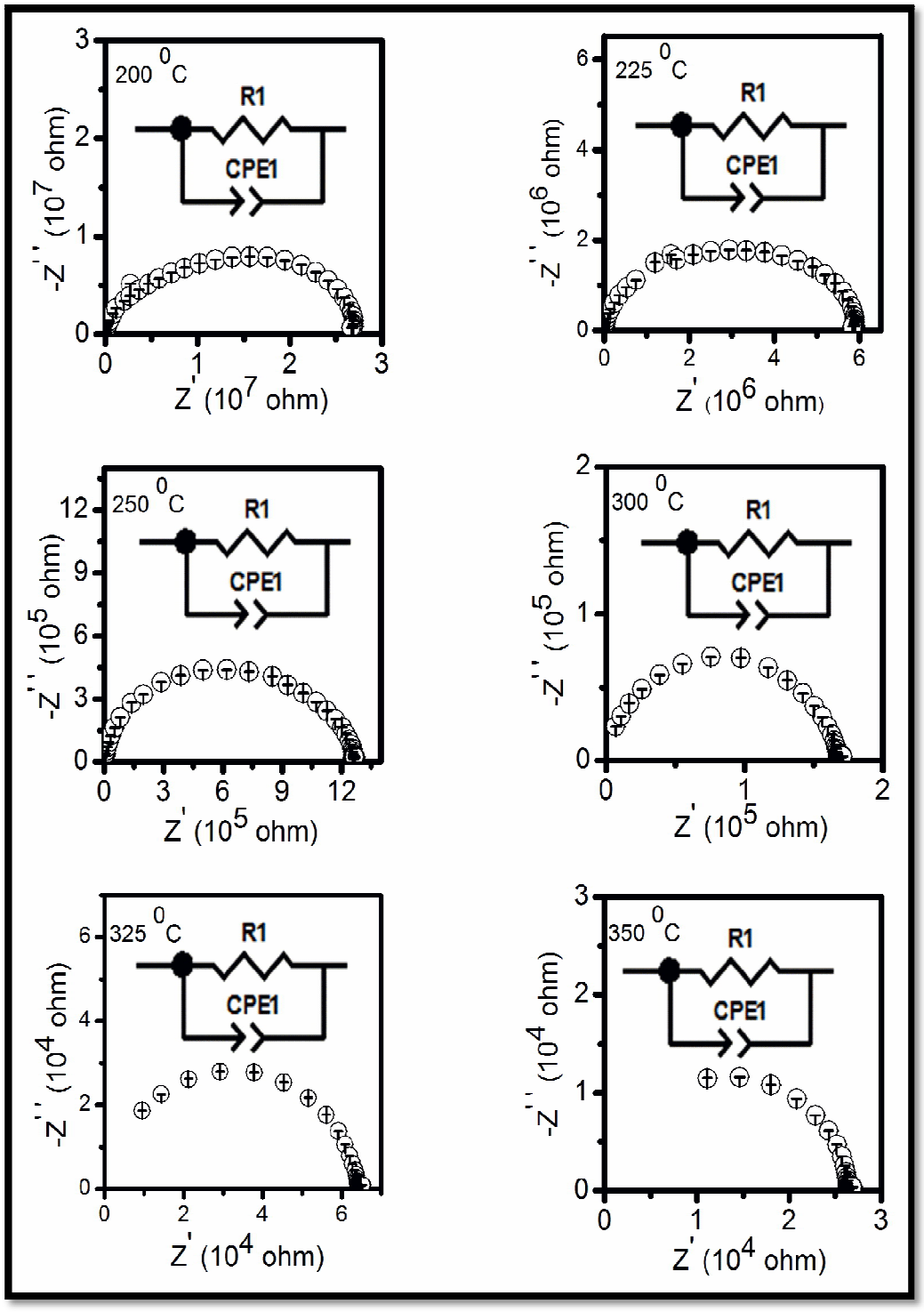

Fig. 4.21 Complex plane impedance plots of the composition LNCO at different temperatures

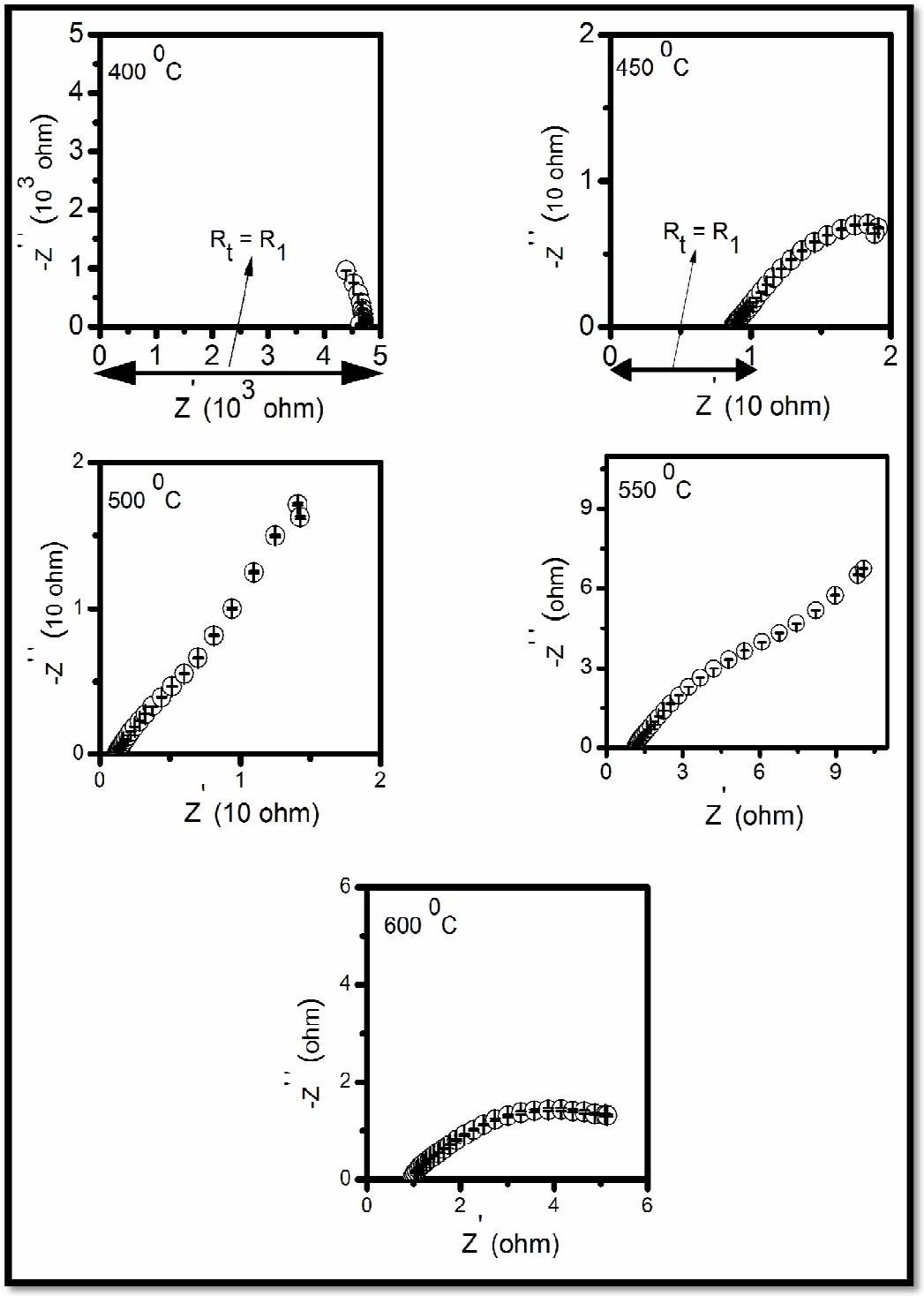

Fig. 4.21 Complex plane impedance plots of the composition LNCO at different temperatures

Fig. 4.22 shows Arrhenius plots of total conductivity for CL7S4/LNCO nanocomposites along with those of CL7S4 and LNCO. In the case of LNCO, a linear behavior in the conductivity plot has been observed up to 425 °C and a jump is observed around 450 °C. This is related to the softening of the carbonates. It is noted from Fig. 4.22 that a sharp increase in the conductivity is observed at 400 ºC for the composites. It is referred to as superionic phase transition at the interfaces [Schober (2005)]. The transition temperature is lower than the melting temperature of the carbonate mixture due to interaction between ceria and carbonate phases. This leads to the threshold percolation to form a highly conducting continuous path at the interfaces below the melting temperature [Huang et al. (2007)]. The interfaces formed between ceria and carbonate phases in the composites have no structural limits and have more cationic defects than that in the bulk.

Below the transition point, conductivity of the composites is less than that of CL7S4. This is because migration of O^{2-} ions is blocked by the dispersed solid amorphous carbonate phase. Conductivity of the composites is higher than that of CL7S4 and LNCO above the transition temperature and increases with increasing carbonate content. This is attributed to conduction of O^{2-} ions through the interfaces in addition to the bulk due to interaction between CL7S4 and LNCO phases [Wang et al. (2010); Di et al. (2010); Zhu et al. (2008)]. Conductivity of the composite with higher content of carbonates i.e. >35 wt% has not been investigated because these contain a large volume of the liquid. This may be deleterious for the measurements.

Above the transition point, concentration of ionic defects in the interfaces and constituent phases increases due to melting from the sublattice to the bulk [Huang et al. (2007)]. In the molten carbonate phase, O^{2-} conduction occurs due to equilibrium between CO_3^{2-} and O^{2-} ions as given below [Zhao et al. (2012); Wang et al. (2011)]

$$CO_3^{2-} \leftrightarrow CO_2 + O^{2-} \tag{4.16}$$

Therefore, the carbonate phase also provides a conducting path for O^{2-} ions in addition to ceria phase. After melting, carbonates fill in the interspaces.

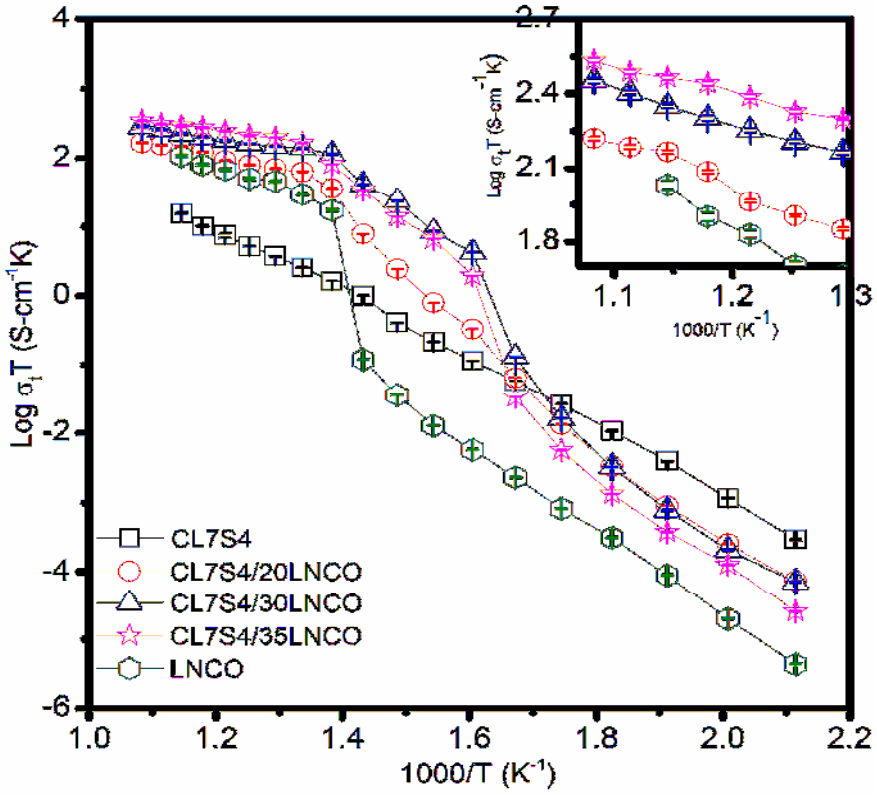

Fig. 4.22 Arrhenius plots of total conductivity for all the compositions in the system CL7S4/LNCO nanocomposites

This generates more interface regions for transport of the ions. Conduction mechanism in composite electrolytes is explained using the theory of defect chemistry [Huang et al. (2010); Bhoga et al. (1998)]. O^{2-} ion conduction in doped ceria occurs by migration of oxygen ions through oxygen ion vacancies generated by doping of La_2O_3 and SrO in CeO_2 as follows:

$$La_2O_3 \xrightarrow{2CeO_2} 2La'_{Ce} + 3O_O^{\times} + V_{\ddot{O}} \tag{4.17}$$

$$SrO \xrightarrow{CeO_2} Sr''_{Ce} + 2O_O^{\times} + V_{\ddot{O}} \tag{4.18}$$

where the symbols are used in accordance with Kroger Vink notation of defects. In the presence of carbonates, oxygen ions may accumulate on the surface resulting in higher concentration of oxygen vacancies in the bulk due to interfacial interaction.

$$O_O^X + V_S \leftrightarrow V_O^{\cdot\cdot} + O_S'' \tag{4.19}$$

In the case of alkali carbonates (M_2CO_3, M = Li, Na and K) phase, a reaction occurs on the surface of the bulk as follows:

$$M_M^X + V_S \leftrightarrow M_S^{\cdot} + V_M' \quad (4.20)$$

$$M_S^{\cdot} + V_i \leftrightarrow M_i^{\cdot} + V_M' \quad (4.21)$$

Subscripts M, S, and i represent the regular M lattice site, surface site and interstitial site respectively. This reaction increases M^+ ion concentration on the surface of one grain and equivalent number of M^+ ion vacancies on the surface of the adjacent grain [Bhoga et al. (1998)]. This may form a space charge layer on the surface of ceria/carbonate phases which enhances the rate of cation disorder reaction [given by equation (4.19) and (4.20)] leading to enrichment of cations at the interfaces. Huang et al. [Huang et al. (2007)] argued that cationic defect concentration is much higher in the space charge zones near phase boundaries than that in the bulk. At the interfaces, defect reactions are given below:

$$M_M^{\cdot} + V_A \leftrightarrow M_A^{\cdot} + V_M' \quad (4.22)$$

$$M_A^{\cdot} + V_i \leftrightarrow M_i^{\cdot} + V_A' \quad (4.23)$$

where, 'A' denotes the interface site. Conductivity of CL7S4/35LNCO composite is 2.56×10^{-1} S/cm at 500 ºC which is much higher than the value of 4.75×10^{-3} S/cm observed in CL7S4 at the same temperature. This value is also higher than 0.01 S/cm reported for $Ce_{0.8}Sm_{0.1}Nd_{0.1}O_{1.9}/(Li/Na)_2CO_3$ by Liu et al. at 481 ºC [Liu et al. (2010)]. Enhancement in the conductivity with the carbonate concentration is also explained using percolation model. According to this model, the electrical conductivity of the composites varies linearly with the volume fraction of the molten carbonate phase. The relation between the conductivity and molten carbonate content is given by Archie equation as given below [Mizuhata et al. (2007)]:

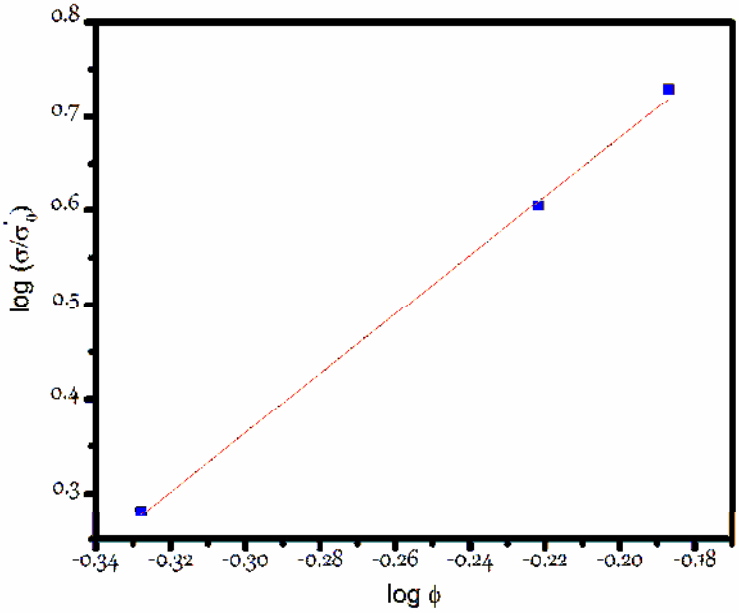

Fig. 4.23 Archie plot for the composite in the system CL7S4/LNCO

$$\frac{\sigma}{\sigma_0'} = a\emptyset^m \tag{4.24}$$

where σ, σ_0', a, φ and m are the total measured conductivity, conductivity of the carbonates, a constant, molten salt content and cementation index respectively. Cementation index represents the solid packing circumstance and depends on the interaction between the solid phase and the molten carbonate phase. Archie plot of the CL7S4/LNCO composites is shown in Fig. 4.23. It has been observed that logarithm of total conductivity of CL7S4/LNCO composites normalized by the conductivity of carbonates varies linearly with logarithm of volume fraction of molten carbonate phase.

Activation energy of conduction determined by fitting the conductivity data to Arrhenius equation is given in Table.4.4. Below the transition point, the activation energy is more in all the composites than that of CL7S4. This may be due to blocking of oxide ions by solid carbonate phase at lower temperatures. Activation energy for CL7S4/35LNCO above the transition point is 0.23 eV.

Table. 4.4 Total conductivity at 500 °C, activation energy and pre-exponential factor (σ_0) for all the samples

S. No.	Compositions	σ_t at 500 °C S/cm	E_a for T > 400 °C (eV)	σ_0
1.	CL7S4	4.75×10^{-3}	0.91 (200-500 °C)	6.31×10^{06}
2.	LNCO	4.73×10^{-2}	0.30	3.05×10^{06}
3.	CL7S4/20LNCO	9.13×10^{-2}	0.35	5.62×10^{09}
4.	CL7S4/30LNCO	1.88×10^{-1}	0.25	2.18×10^{10}
5.	CL7S4/35LNCO	2.56×10^{-1}	0.23	1.32×10^{11}

This is much smaller than 0.89 eV obtained by Li et al. [Li et al. (2007)]. This is also in conformity with the value of activation energy (<0.2 eV) obtained by Zhu et al. (2008) for interfacial conduction of O^{2-} ions. This may be due to easier migration of O^{2-} ions through the interface than that in the bulk ceria phase. It is noted from Table. 4.4 that the value of pre-exponential factor is also more for the composites as compared to CL7S4 and LNCO. This confirms that composites have large number of mobile ions and long jump distance at the interfaces. Therefore, it is concluded that above the transition point, conductivity of the composite electrolytes is predominantly due to interfacial conduction of the ions. This results in low activation energy and high ionic conductivity.

4.2.3 Conclusion

- Nanocomposites of, $Ce_{0.89}La_{0.07}Sr_{0.04}O_{1.925}$ with varying amount of $(Li\text{-}Na)_2CO_3$ have been prepared successfully.
- Single phase formation has been observed in all the composites. Micrographs show homogeneous distribution of both the phases with ceria grains surrounded by amorphous carbonate phase.
- Impedance spectroscopy shows that the charge transport in the composites is different from that in the single phase ceria based electrolytes.

- A sharp increase in the conductivity occurs at 400 ºC. This is attributed to superionic transition at the interfaces.
- Composite, CL7S4/35LNCO shows the maximum conductivity of 2.56×10^{-1} S/cm at 500 ºC.
- Activation energy of conduction in CL7S4/35LNCO composite is found to be 0.23 eV. This is in confirmation with the interfacial conduction of oxide ions.